# Destabilizing resonances of precessing inertia-gravity waves

N. Benkacem, A. Salhi, A. Khlifi, S. Nasraoui, Claude Cambon

# Destabilizing resonances of precessing inertia-gravity waves

N. Benkacem,[1] A. Salhi,[2,3] A. Khlifi,[1] S. Nasraoui,[1,4] and C. Cambon[2]

[1]*Université de Tunis El Manar, Faculté des Sciences de Tunis, Laboratoire Matériaux Organisation et Propriétés, 2092 Tunis, Tunisie*

[2]*Université de Lyon, Laboratoire de Mécanique des Fluides et d'Acoustique, UMR 5509, Ecole Centrale de Lyon, CNRS, UCBL, INSA F-69134 Ecully Cedex, France*

[3]*Département de Physique, Faculté des Sciences de Tunis, 2092 Tunis, Tunisia*

[4]*Department of Civil and Environmental Engineering, Hong Kong University of Science and Technology, Kowloon, Hong Kong 999077, China*

(Received 12 February 2021; revised 3 November 2021; accepted 15 February 2022; published 16 March 2022)

Instabilities in stratified precessing fluid are investigated. We extend the study by Mahalov [Phys. Fluids A **5**, 891 (1993)] in the stably stratified Boussinesq framework, with an external Coriolis force (with rate $\Omega_p$) altering the base flow through the distortion of the circular streamlines of the unperturbed axially stratified rotating columns (with constant vorticity $2\Omega$). It is shown that the inviscid part of the modified velocity flow $(0, \Omega r, -2\varepsilon\Omega r \sin\varphi)$ and buoyancy with gradient $N^2(-2\varepsilon\cos\varphi, 2\varepsilon\sin\varphi, 1)$ are an exact solution of Boussinesq-Euler equations. Here $(r, \varphi, z)$ is a cylindrical coordinate system, with $\varepsilon = \Omega_p/\Omega$ being the Poincaré number and $N$ the Brunt-Väisälä frequency. The base flow is transformed into a Cartesian coordinate system, and the stability of a superimposed perturbation is studied in terms of Fourier (or Kelvin) modes. The resulting Floquet system for the Fourier modes has three parameters: $\varepsilon$, $\mathcal{N} = N/\Omega$, and $\mu$, which is the angle between the wave vector $\boldsymbol{k}$ and the solid-body rotation axis in the limit $\varepsilon = 0$. In this limit, there are inertia-gravity waves propagating with frequency $\pm\omega$ and the resonant cases are those for which $2\omega = n\Omega$, $n$ being an integer. We perform an asymptotic analysis to leading order in $\varepsilon$ and characterize the destabilizing resonant case of order $n = 1$ (i.e., the subharmonic instability) which exists and for $0 \leqslant N < \Omega/2$. In this range, the subharmonic instability remains the strongest with a maximal growth rate $\sigma_m = [\varepsilon(5\sqrt{15}/8)\sqrt{1-4\mathcal{N}^2}/(4-\mathcal{N}^2)]$. Stable stratification acts in such a way as to make the subharmonic instability less efficient, so as it disappears for $N \geqslant 0.5\Omega$. The destabilizing resonant cases of order $n = 2, 3, 4, 5$ are investigated in detail by numerical computations. The effect of viscosity on these instabilities is briefly addressed assuming the diffusive coefficients (kinematic and thermal) are equal. Likewise, we briefly investigate the case where $N^2 < 0$ and show that the instability associated to the mode with $k_3 = 0$ is the strongest.

DOI: 10.1103/PhysRevE.105.035107

## I. INTRODUCTION

Several planets and celestial bodies are characterized by self sustained magnetic fields due to dynamos in action within their fluid cores. The motions underlying the dynamo process can be induced by mechanical driving mechanisms, especially the precession, which has been explored in numerous studies (see, e.g., Refs. [1–9]). Precession consists in the rotation of the axis of a rotating flow. In a precessing domain, the dynamics of the flow results therefore from the interplay between inertial waves, Ekman boundary layers, and large scale motions however complex (see Ref. [10]). The flow can eventually become unstable and develop a fully develop turbulent state with structures at all the scales filling the spatial domain (see Refs. [2,9]). In geophysical and astrophysical frameworks the turbulence driven by precession is able to support the conversion of huge amounts of kinetic to magnetic energy, and to sustain the generation of magnetic field like in the Earth's outer core (see Ref. [2]). Precession can also trigger instabilities leading to the formation of vortex tangles and it can generate turbulence in superfluid neutron star interiors (see Ref. [11]).

### A. Generic precessing flows

The case of rotating columns in a fluid on which is acting an external Coriolis force represents a simple example of precessing flows. Mahalov [12] showed that the Coriolis force alters the base flow by distorting circular streamlines of the unperturbed rotating fluid columns. In particular, making the analogy with the elliptical cylinder [13,14], Mahalov considered the basic inviscid flow

$$\boldsymbol{U} = (\Omega r)\boldsymbol{e}_\varphi - 2(\varepsilon\Omega r \sin\varphi)\boldsymbol{e}_3 \tag{1}$$

within an infinite cylinder precessing at

$$\boldsymbol{\Omega}_p = \varepsilon\Omega(\cos\varphi\boldsymbol{e}_r - \sin\varphi\boldsymbol{e}_\varphi),$$
$$\boldsymbol{W}_a = \nabla\times\boldsymbol{U} + 2\boldsymbol{\Omega}_p = 2\Omega\boldsymbol{e}_3,$$

where $\Omega$ is the (constant) rotation rate, $\varepsilon = \Omega/\|\boldsymbol{\Omega}_p\|$ is the Poincaré number which gives the relative frequencies of precessional to diurnal rotation and controls the strength of the precessional forcing. A negative $\varepsilon$ refers to retrograde precession (as is the case for planets). Here, $\boldsymbol{W}_a$ denotes the basic absolute vorticity and $(\boldsymbol{e}_r, \boldsymbol{e}_\varphi, \boldsymbol{e}_3)$ is a direct orthonormal basis associated with the cylindrical coordinate system $(r, \varphi, x_3)$

 

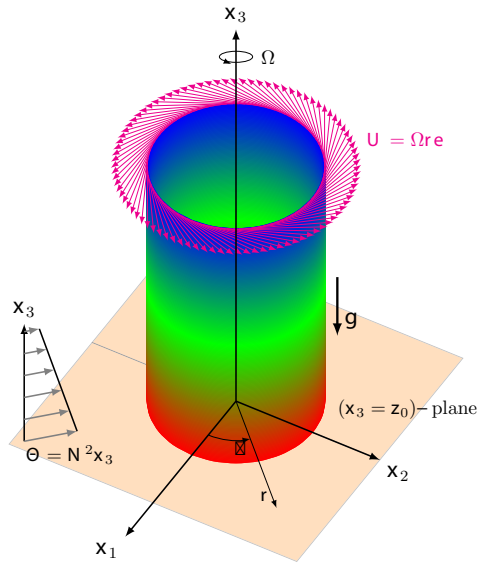


FIG. 1. A stratified rotating fluid column of radius $r_0$ about the $x_3$ axis. The rotation rate is $\Omega = \text{cste} > 0$. The flow streamlines are then circles of radius $r \leqslant r_0$ and of axis $x_3$, $x_1^2 + x_2^2 = r^2$, with $x_1 = r\cos\varphi$, $x_2 = r\sin\varphi$, and $\varphi = \Omega t$. The figure shows a slice of this stratified rotating column between the planes $x_3 = z_0$ and $x_3 = z_1$ where $z_1 > z_0$. The unperturbed velocity profile, $\boldsymbol{U} = \Omega r \boldsymbol{e}_\varphi$, normalized by $\Omega r_0$, is shown in the $z_1$ plane for the streamline of radius $r_0$. The color variation of the streamlines (from red to blue) represents the linear variation of the buoyancy scalar, $\Theta = N^2 x_3$, as a function of $x_3$, with $N^2 > 0$ (stable stratification) where $N$ is the Brunt-Väisälä frequency. The gravity vector $\boldsymbol{g}$ is then given by $\boldsymbol{g} = -g\boldsymbol{e}_3$, with $g > 0$. Schematic of the unperturbed buoyancy scalar, $\Theta = N^2 x_3$, is also shown.

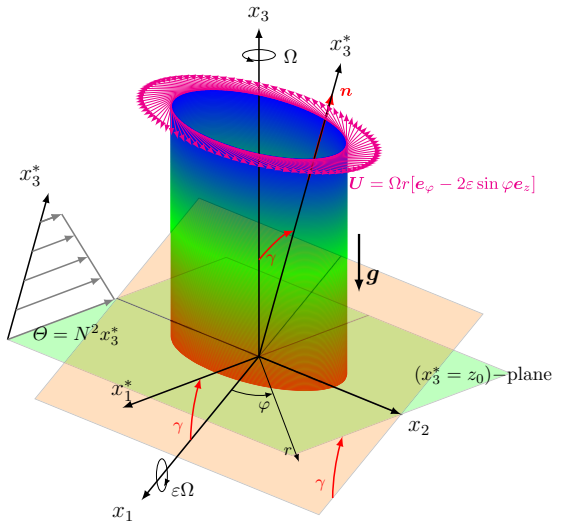


FIG. 2. A stratified precessing fluid column: The rotating fluid column shown in Fig. 1 is now rotating about the $x_1$ axis with rate $\Omega_p = \varepsilon\Omega$ where $\varepsilon$ is the Poincaré number. The effect of the Coriolis force induces a vertical mean shear that acts to balance the gyroscopic torque. The trajectory of a fluid particle is given by $x_1^2 + x_2^2 = r^2 = \text{cste}$, $\varphi = \Omega t$ and $x_3 = 2\varepsilon r\cos\varphi + \text{cste} = 2\varepsilon x_1 + \text{cste}$. Since the difference $(x_3 - 2\varepsilon r\cos\varphi) = (x_3 - 2\varepsilon x_1)$ is time-independent, the trajectory of a fluid particle is in the plane perpendicular to the axis $x_3^* = (x_3 - 2\varepsilon x_1)/\sqrt{1+4\varepsilon^2} = \text{cste}$ and it is an ellipse, $(x_1^* - 2\varepsilon x_3^*)^2/(1+4\varepsilon^2) + x_2^{*2} = \text{cste}$, where $x_1^* = (x_1 + 2\varepsilon x_3)/\sqrt{1+4\varepsilon^2}$ and $x_2^* = x_2$ (see Sec. IIA2). The plane $(x_1^*, x_3^*)$ is obtained by a rotation, of angle $\gamma = -\tan^{-1}(2\varepsilon)$, of the plane $(x_1, x_3)$ around the $x_2$ axis. The unperturbed velocity profile, $\boldsymbol{U} = \Omega r(\boldsymbol{e}_\varphi - 2\varepsilon\sin\varphi\boldsymbol{e}_3)$, normalized by $\Omega r_0$, is shown in the $(x_3^* = z_1)$ plane for the ellipse having $r_0$ as the semiminor axis and $r_0\sqrt{1+4\varepsilon^2}$ as the semimajor axis. In describing its elliptic trajectory the fluid particle moves upward when $0 \leqslant \varphi < \frac{\pi}{2}$ or $\frac{3\pi}{2} < \varphi \leqslant 0$ and down when $\frac{\pi}{2} < \varphi < \frac{3\pi}{2}$. Therefore, in the case with precession each one of the planes $x_3^* = \text{cste}$ is a plane of isodensity, so that $\Theta = N^2 x_3^* = N^2(-2\varepsilon r\cos\varphi + x_3) = N^2(-2\varepsilon x_1 + x_3)$. Schematic of the unperturbed buoyancy scalar, $\Theta = N^2 x_3^*$, is also shown. The unit vector $\boldsymbol{n} = \nabla\Theta/\|\nabla\Theta\|$ aligns with the $x_3^*$ axis.

(see Figs. 1 and 2). The inviscid component of the modified flow (i.e., the basic flow Eq. (1), hereinafter referred to as MHF) is an exact solution of the Euler equations.

A physical interpretation of the modified flow can be found here, as also in Salhi and Cambon [15]: the misalignment of the basic "rapid" angular velocity $\boldsymbol{\Omega} \equiv (\nabla \times \boldsymbol{U})(\varepsilon = 0)$ and the precessional one $\boldsymbol{\Omega}_p$, treated as an external Coriolis force, induces a gyroscopic torque. This torque can be exactly balanced by the plane shear (i.e., the second term in the right hand side of Eq. (1) or $\boldsymbol{U}_s = -2\varepsilon r\Omega\sin\varphi\boldsymbol{e}_3$). The induced shear is emphasized in previous experimental studies (see, e.g., Vladimirov and Tarasov [16], Wiener *et al.* [17], Mouhali *et al.* [8]), not to mention its close connection with more complex flow patterns. For instance, Wiener *et al.* [17] presented experimental investigations of Taylor vortex flow under the effect of an external Coriolis force. observing the transition to turbulence for larger rotation rates. Mahalov [12] conjectured that this transition is indicative of parametric (precessional) instabilities developing within the flow.

In terms of a normal mode stability analysis, the disturbances superimposed to MBF take the form $\sim \exp\mathrm{i}(m\varphi + lx_3 + \omega t)$, where $m$ and $l$ are integers), a local (precessional) instability occurs when two inertial modes of the system, $(\omega_1, m_1, l_1)$ and $(\omega_2, m_2, l_2)$, are resonantly coupled by the underlying strained state, $(\omega, m, l) = (0, 1, 0)$ (see Refs. [12,18]),

$$\omega_1 - \omega_2 = 0, \quad m_2 - m_1 = 1, \quad l_2 - l_1 = 0.$$

We would like to point out that the only boundary condition implemented in the study by Mahalov [12] consist in having no flow through the boundaries. We also note that the (precessional) instability mechanism is here similar to the one of the elliptical instability as conjectured by Malkus [19]. The term "elliptical instability" is the name given to the linear instability mechanism by which three-dimensional flows can be generated in regions of two-dimensional, elliptical streamlines [18]. Its mechanism is also one of resonance in which a pair of normal modes of oscillation on the undistorted circular flow become tuned to the underlying strain field (so that, $m_2 - m_1 = 2$, see, e.g., Refs. [14,18]). Elliptical flow ($m = 2$) and precessing flow ($m = 1$) are examples of a a class of nonaxisymmetric rotating flows with $\exp(\mathrm{i}m\varphi)$-dependent asymmetries.

The findings by Mahalov [12] for waves traveling in the precessing infinite cylinder are consistent with those by

Kerswell [4] for waves traveling in a rotating unbounded fluid whose rotation axis is precessing. The undisturbed, steady state considered by Kerswell consists of sheared circular streamlines,

$$\boldsymbol{U} = \mathbf{A}\cdot\boldsymbol{x}, \quad \mathbf{A} = \Omega\begin{pmatrix} 0 & -1 & 0 \\ 1 & 0 & -2\varepsilon \\ 0 & 0 & 0 \end{pmatrix},$$
$$\boldsymbol{W}_a = 2\Omega(2\varepsilon, 0, 1)^T, \tag{2}$$

where $(x_1, x_2, x_3)$ is a Cartesian coordinate system associated to the direct orthonormal basis $(\boldsymbol{e}_1, \boldsymbol{e}_2, \boldsymbol{e}_3)$ and $T$ denotes transpose. This basic velocity has been derived from the so-called Poincaré solution, characterizing the response of an inviscid fluid within a precessing, oblate spheroid.

The "unbounded" analysis by Kerswell [4] consists in the use of perturbations in terms of Lagrangian Fourier modes (sometime called Kelvin's mode, $\sim \exp \mathrm{i}\boldsymbol{k}(t)\cdot\boldsymbol{x}$) where $\boldsymbol{k}(t)$ is the time-dependent wave vector [20,21]), in agreement with an unbounded, or extensional, base flow. For extensional flows, the use of Fourier modes with time-dependent wave vector, or Lagrangian Fourier modes, reflects the conservation of the phase of the Fourier modes, or $\boldsymbol{k}\cdot\boldsymbol{x} = \boldsymbol{k}_0\cdot\boldsymbol{x}_0$, where $\boldsymbol{x}_0$ refers to the Lagrangian position of the mean, or base-flow, trajectory, with $\boldsymbol{k}_0$ its wave-vector counterpart (details in Sagaut and Cambon [22]). More generally and perhaps more explicitly, the zonal theory of Lifschitz and Hameiri [23] implies the conservation of phase $\Phi$, or $\boldsymbol{k}\cdot\delta\boldsymbol{x} = \boldsymbol{k}_0\cdot\delta\boldsymbol{x}_0$ for a wave packet following any smooth base-flow trajectory, with any base-flow gradient. In this case the wave-vector, as the gradient of the phase, depends on both time and position. In short, the wave-vector is moving for having a nonmoving phase.

Kerswell's "unbounded" analysis, which is in effect an idealisation of a small scale perturbation evolving in the center of a precessing spheroid, explored the local precessional instability confirming that, in this case, the effect of boundaries is mostly secondary.

### B. Stratified precessing flows

The effect of an axial stable density stratification on Taylor columns has been previously investigated experimentally and theoretically (see, e.g., Davies [24]). Caton *et al.* [25] studied stability and bifurcations in a flow between two concentric cylinders, with the inner one rotating, in the presence of an axial stable density stratification (i.e., a stratified Taylor-Couette flow). Hollerbach [26] investigated numerically the instabilities of Taylor columns in a rotating stratified fluid, considering a flow in a differentially rotating spherical shell, with stable stratification imposed along the rotation axis.

Here we intend to extend Mahalov's theoretical study by including the effect of stratification. In the Boussinesq approximation and without precession ($\varepsilon = 0$), we find that

$$\boldsymbol{U} = \Omega r\boldsymbol{e}_\varphi, \tag{3a}$$
$$\Theta \equiv -(g/\rho_0)\varrho = N^2 x_3, \tag{3b}$$
$$\boldsymbol{n} \equiv \frac{\boldsymbol{\nabla}\Theta}{\|\boldsymbol{\nabla}\Theta\|} = \boldsymbol{e}_3, \tag{3c}$$

is a solution of the Boussineq-Euler equations [see Eq. (7)]. The flow described by these equations corresponds to unperturbed rotating columns with axial constant stratification $N^2$ (see Fig. 1). Here, $\varrho$ indicates the basic density, $\rho_0$ a fixed reference density, $g$ the gravity acceleration, and $\Theta\boldsymbol{n}$ the unperturbed buoyancy force per unit mass. For $\varepsilon \neq 0$, a correction to the basic flow Eq. (3) is needed to fulfill the so called "admissibility" conditions (i.e., the base flow must be a solution of the Boussinesq-Euler equations [27]). Without stratification, Mahalov [12] proposed a correction to the basic velocity Eq. (3a) that yields the solution Eq. (1). In the presence of stratification, in a similar fashion, we implement a correction to the basic buoyancy scalar field that yields the following solution (see Appendix A and Fig. 2),

$$\Theta = N^2(-2\varepsilon r\cos\varphi + x_3), \tag{4a}$$
$$\boldsymbol{n} = \frac{1}{\sqrt{1+4\varepsilon^2}}[-2\varepsilon(\cos\varphi\boldsymbol{e}_r - \sin\varphi\boldsymbol{e}_\varphi) + \boldsymbol{e}_3]. \tag{4b}$$

Accordingly, one finds that the base flow, coupling the basic velocity described by Eq. (1) and the basic buoyancy scalar described by Eq. (4), is an exact solution of the Boussinesq-Euler equations [see Eq. (7)]. The presence of the additional horizontal component of the mean density gradient, which vanishes in the case without precession ($\varepsilon = 0$), is thereby due to the gyroscopic torque as for the additional mean shear. This point is one of the original results proposed in the present study.

We note that in some recent studies, buoyancy forcing has been taken into account together with precession. Wei and Tilgner [28] considered a fixed uniform background radial stratification in a spherical shell with a small stress-free inner core (see also Ref. [29]). They found that stable stratification can suppress possible precessional instabilities and becomes relevant if the ratio of the Brunt-Väisälä frequency $N$ to the rotation rate $\Omega$ is near 1. However, unstable stratification ($N^2 < 0$) and precession can either stabilize or destabilize each other at different precession rates.

### C. Extended linear stability approach and beyond

Following the findings by Mahalov [12] and Kerswell [4], as indicated previously, we transform the solution stemming from Eqs. (1) and (4) into a Cartesian coordinate system,

$$\boldsymbol{U} = \mathbf{A}\cdot\boldsymbol{x}, \quad \mathbf{A} = \Omega\begin{pmatrix} 0 & -1 & 0 \\ 1 & 0 & 0 \\ 0 & -2\varepsilon & 0 \end{pmatrix}, \quad \boldsymbol{W}_a = 2\Omega\boldsymbol{e}_3, \tag{5a}$$
$$\Theta = N^2(-2\varepsilon x_1 + x_3), \tag{5b}$$
$$\boldsymbol{n} = \frac{1}{\sqrt{1+4\varepsilon^2}}(-2\varepsilon\boldsymbol{e}_1 + \boldsymbol{e}_3), \tag{5c}$$

and perform a stability analysis for the perturbations to that base flow. Similarities and differences between the Kerswell's base flow and the Mahalov's base flow are mentionned in Sec. IIA3.

Perturbations to the rotating stratified flow, recovered here at $\varepsilon = 0$, are propagating inertia-gravity waves with dispersion frequency,

$$\omega_{1,2} = \pm\sqrt{\omega_r^2 + \omega_g^2}, \tag{6}$$

where $\omega_r = \pm 2\boldsymbol{\Omega}\cdot\boldsymbol{k}/\|\boldsymbol{k}\|$ is the frequency of inertial waves and $\omega_g = \pm N\|\boldsymbol{e}_3 \times \boldsymbol{k}\|/\|\boldsymbol{k}\|$ is the frequency of gravity waves. The inertia-gravity waves resonant cases, i.e., those for which $\omega = n\Omega$ with $n$ an integer number, characterize the onset of linear instability, hence are analyzed in detail (see Sec. IV).

Here we introduce the framework of the present study, where a base (or mean) flow is defined and the linear analysis of the perturbations is implemented in a rather straightforward manner for $\varepsilon \neq 0$. In agreement with extensional base flows with space-uniform gradients, perturbations are treated in terms of Lagrangian Fourier modes instead of normal modes.

The class of flows considered in the exploration of the elliptical flow instability by Bayly [20] and Pierrehumbert [30], was emphasized as "exact solutions" by Craik and Criminale [21] when considering a single-mode disturbance, as in the conventional stability analysis. However, the application to the rapid distortion theory (RDT) allows to treat turbulence at large Reynolds number with a similar linear analysis, when initial fluctuations have a large continuous spectrum gathering several modes. Of course, the "rapid" (short-time) limit ought to be justified, since RDT solutions are no longer exact solutions. Beyond RDT, wave turbulence theory and triadic closures were developed to evaluate the explicit nonlinearity, especially in the case of purely rotating flows, and purely stratified flows, stable and unstable (for a review on closures see Ref. [22].) Last but not least, the linear theory is often used as building block of the fully nonlinear approach: for instance, nonlinearity is *implicitly present* in the analysis of regeneration cycles for the study of the shear flows stability, when considering, for instance, the application to the stability of accretion discs (see, e.g., Refs. [31,32]). In this last example, the accretion disk is treated as a Taylor-Couette flow, and the shearing sheet approximation [33] reduces the problem to the study of a base flow with uniform $S$ and $\Omega$ parameters, similar to though simpler than Eq. (5).

Considering explicit nonlinearity, DNS have been carried here in the same context of (statistically) homogeneous turbulence (for fluctuations) under the effect of space-uniform mean velocity gradients and body forces. The analysis of the DNS runs is anticipated by the exploration of a largest range of parameters through the linear analysis, being done to identify the flow regimes which are more relevant for the numerical investigation. In that respect, the precessing flow described by Eq. (5) appears to be particularly suitable to perform DNS of (statistically) homogeneous precessing turbulence. Recent DNS studies (see Refs. [34,35]) have shown that the precessional instability is saturated by nonlinear interactions. Indeed, for an initially homogeneous isotropic turbulence flow characterized, in the presence of a mean flow Eq. (5a), it was found that the temporal evolution of the turbulent kinetic energy $E_\kappa$ occurs in two main phases associated with different flow topologies: (i) an exponential growth characterizing three-dimensional turbulence dynamics and (ii) nonlinear saturation regime during which $E_\kappa$ remains almost time-independent, the flow becoming quasi-two-dimensional. A similar behavior is found in the recent DNS study of a precessing magnetized turbulence by Salhi *et al.* [36].

Because of the close similarity between elliptical and precessional instabilities, it is useful to briefly report here some results characterizing the effects of stratification in unbounded elliptical flows. Miyazaki and Fukumoto [37] considered an unbounded strained-vortex flow with stable stratification. Among more general setups, they choose a very simple stratification profile, i.e., with the density varying exponentially in the $x_3$ direction. This simplification admits a constant Brunt-Väisälä frequency throughout the fluid domain. This points to the fact that the resulting linear differential system for the perturbations superimposed to the base flow, is the same when considering either an exponential mean stratification or a linear mean stratification. Miyazaki and Fukumoto [37] have found that the growth rates for the elliptical instability were invariably reduced. Note that the elliptical instability of stratified vortices has been addressed as well in previous studies (see, e.g., Refs. [37–40]). Recently, Singh and Mathur [41] have studied the effect of the Prandtl number ($\mathrm{Pr} = \nu_v/\kappa$, i.e., the ratio of the kinematic viscosity to the thermal diffusivity) on the elliptical instability, under stable stratification. They showed that $\mathrm{Pr} \neq 1$ influences in a nontrivial way the inviscid instabilities reported by Miyazaki and Fukumoto [37], and also introduces a new branch of oscillatory instability that is not present at $\mathrm{Pr} = 1$. In this study we focus on the case $\mathrm{Pr} = 1$ to reduce the mathematical complexity of the asymptotic analysis.

Concerning the effect of precession on the resonant cases of inertia-gravity waves, there are similarities with and differences from previous work on the effect of stratification on the elliptical instability, as will be shown in the present study. The paper is organized as follows: the Boussinesq equations for the perturbations to the base flow in physical and Fourier spaces are presented in Sec. II; by means of potential vorticity (PV; see Ref. [42]), which is Lagrangian invariant for a nondiffusive fluid, we then derive two-dimensional Floquet systems governing the evolution of the Fourier amplitudes in the linear regime; resonant cases of inertia-gravity waves are then analyzed in Sec. III; the stability analysis of the Floquet systems is presented in Sec. IV, with analytical derivations based on perturbation techniques (see Refs. [43,44]) being implemented together with the numerical computations, and viscosity effects (for $\mathrm{Pr} = 1$) as well as the effect of unstable stratification ($N^2 < 0$) being briefly addressed; Sec. V is finally devoted to concluding remarks.

## II. MATHEMATICAL FORMULATION

### A. The Boussinesq equations

We consider a stratified unbounded inviscid and non diffusive fluid. The effects of viscosity ($\nu_v$) and thermal diffusivity ($\kappa$), such that $\nu_v = \kappa$, so that the Prandtl number $\mathrm{Pr} = \nu_v/\kappa$ is unity, will be briefly addressed at the end of Sec. IV D. The density variations are introduced using the Boussinesq approximation for simplicity.

#### *1. Governing equations*

Boussinesq's equations written in a frame rotating uniformly around a fixed axis are of the form (see Ref. [45])

$$\boldsymbol{\nabla}\cdot\tilde{\boldsymbol{u}} = 0, \tag{7a}$$

$$D_t\tilde{\boldsymbol{u}} = -\boldsymbol{\nabla}\tilde{p} - 2\Omega_p \times \tilde{\boldsymbol{u}} + \tilde{\vartheta}\boldsymbol{n}, \tag{7b}$$

$$D_t\tilde{\vartheta} = 0, \tag{7c}$$

where, $D_t(\cdot) \equiv (\partial_t + \tilde{\boldsymbol{u}}\cdot\boldsymbol{\nabla})(\cdot)$ denotes the material derivative where $t$ denotes time and $\Omega_p$ denotes the rotation vector of the reference frame. Here, $\tilde{p}$ being the total pressure (including the centrifugal potential) divided by the constant density, $\rho_0$. The buoyancy scalar $\tilde{\vartheta}$, which is re-scaled as an acceleration, is proportional to the gravitational acceleration and to the background density (or temperature) gradient. In the precessing frame $(\boldsymbol{e}_1, \boldsymbol{e}_2, \boldsymbol{e}_3)$ defined in Sec. I, the expression of the unit vector $\boldsymbol{n}$ is given by Eq. (5c). Therefore, without precession ($\varepsilon = 0$), $\boldsymbol{n}$ aligns with the solid-body rotation axis, but, in the presence of precession ($\varepsilon \neq 0$), it deviates from this rotation axis at an angle $\gamma = -\tan^{-1}(2\varepsilon)$ (see also Fig. 1).

We denote by

$$\tilde{\varpi}_\kappa = \tilde{\boldsymbol{\omega}}_a\cdot\boldsymbol{\nabla}\tilde{\vartheta} \tag{8}$$

the potential vorticity (PV, see Ref. [42]), which is a Lagrangian invariant, i.e., $D_t\tilde{\varpi}_\kappa = 0$ for a non diffusive fluid. Here, $\tilde{\boldsymbol{\omega}}_a = \boldsymbol{\nabla}\times\tilde{\boldsymbol{u}} + 2\boldsymbol{\Omega}_p$ being the instantaneous absolute vorticity,

#### 2. Mahalov's base flow

The solutions of system Eq. (7) are conveniently decomposed into a 'basic flow' $(\boldsymbol{U}, P, \Theta)$ and a 'disturbance' $(\boldsymbol{u}, p, \vartheta)$,

$$\tilde{\boldsymbol{u}} = \boldsymbol{U} + \boldsymbol{u}, \quad \tilde{p} = P + p, \quad \tilde{\vartheta} = \Theta + \vartheta. \tag{9}$$

The base flow mainly considered in the present study, especially for analytical developments, is the Mahalov's base flow, which was introduced in Sec. I, and also reported here, for the sake of clarity,

$$\boldsymbol{U} = \mathbf{A}\cdot\boldsymbol{x}, \quad \mathbf{A} = \Omega\begin{pmatrix}0 & -1 & 0\\ 1 & 0 & 0\\ 0 & -2\varepsilon & 0\end{pmatrix}, \quad \boldsymbol{W}_a = 2\Omega\boldsymbol{e}_3, \tag{10a}$$

$$\Theta = N^2(-2\varepsilon x_1 + x_3), \tag{10b}$$

$$\boldsymbol{n} = \frac{1}{\sqrt{1+4\varepsilon^2}}(-2\varepsilon\boldsymbol{e}_1 + \boldsymbol{e}_3). \tag{10c}$$

It is informative to determine and to discuss the trajectory of a fluid particle for the Mahalov's base flow (MBF). Let $(x_{01}, x_{02}, x_{03})$ and $(x_1, x_2, x_3)$ be the positions of a fluid particle at times $t = 0$ and $t > 0$, respectively. The trajectory of a fluid particle is obtained by integrating the equation $\boldsymbol{U} = d\boldsymbol{x}/dt = \mathbf{A}\cdot\boldsymbol{x}$, so that

$$x_1(\tau) = r_0\cos(\tau + \alpha), \tag{11a}$$

$$x_2(\tau) = r_0\sin(\tau + \alpha), \tag{11b}$$

$$x_3(\tau) = x_{30} + 2\varepsilon(x_1 - x_{10}), \tag{11c}$$

where $\tau = \Omega t$ is a dimensionless time, $r_0 = \sqrt{x_{10}^2 + x_{20}^2}$ and $\alpha = \tan^{-1}(x_{20}/x_{10})$. The trajectory of a fluid particle is then an ellipse, as shown below (see also Fig. 2). Equation (11c) indicates that the difference $(x_3 - 2\varepsilon x_1)$ is time-independent. Therefore, the trajectory is in a plane perpendicular to the axis $x_3^*$ defined by

$$x_3^* = \frac{1}{\sqrt{1+4\varepsilon^2}}(x_3 - 2\varepsilon x_1). \tag{12}$$

To find the planes perpendicular to the axis $x_3^*$, we use the fact that this axis is in the plane $(x_1, x_3)$, and we then determine the axis $x_1^*$ belonging to this plane and which is perpendicular to the axis $x_3^*$. The result is

$$x_1^* = \frac{1}{\sqrt{1+4\varepsilon^2}}(x_1 + 2\varepsilon x_3). \tag{13}$$

The plane $(x_1^*, x_3^*)$ is obtained by a rotation, of angle $\gamma = -\tan^{-1}(2\varepsilon)$, of the plane $(x_1, x_3)$ around the $x_2$ axis. Therefore, in terms of the variables $(x_1^*, x_2^*, x_3^*)$, Eq. (11) can be rewritten in the following form

$$\frac{(x_1^* - 2\varepsilon x_3^*)^2}{r_0^2(1+4\varepsilon^2)} + \frac{x_2^{*2}}{r_0^2} = 1 \quad \text{with} \quad x_3^* = \text{cste}, \tag{14}$$

which clearly shows that the trajectory of a fluid particle is an ellipse. The ellipse has $r_0$ as the semiminor axis and $r_0\sqrt{1+4\varepsilon^2}$ as the semimajor axis (see Fig. 2).

#### 3. Kerswell's base flow

Although there is a close similarity between the MBF and the Kerswell's base flow (KBF), some differences between these two base flows can be pointed out. Recall that the KBF [given by Eq. (5)] is derived from the so-called Poincaré solution, characterizing the response of an inviscid fluid within a precessing, oblate spheroid [4].

The KBF is with horizontal shear (its cross-gradient direction is normal to both main and precessing angular velocities) and the absolute vorticity vector $\boldsymbol{W}_a = 2\Omega(-2\varepsilon\boldsymbol{e}_1 + \boldsymbol{e}_3)$ deviates from the main rotation axis. The flow streamlines are circles that are sheared across each other (see also Kerswell [4]),

$$(x_1 + 2\varepsilon x_3)^2 + x_2^2 = r_{0\varepsilon}^2, \quad x_3 = x_{30}, \tag{15}$$

where $r_{0\varepsilon} = \sqrt{(x_{10} + 2\varepsilon x_{30})^2 + x_{20}^2}$. However, the MBF is with vertical shear (its cross-gradient direction is aligned with the main angular velocity) and the absolute vorticity vector $\boldsymbol{W}_a = 2\Omega\boldsymbol{e}_3$ aligns with the main rotation axis. The flow streamlines are ellipses [see Eq. (14)]. However, even with these differences, a linear stability analysis in terms of Fourier modes gives the same result for the two basic flows if we limit ourselves to the first order in $\varepsilon$. Indeed, by applying the coordinate transformation described by Eqs. (12) and (13) to the MBF, we obtain

$$\boldsymbol{U} = \mathbf{A}\cdot\boldsymbol{x}, \quad \mathbf{A} = \frac{\Omega}{\sqrt{1+4\varepsilon^2}}\begin{pmatrix}0 & -(1+4\varepsilon^2) & 0\\ 1 & 0 & -2\varepsilon\\ 0 & 0 & 0\end{pmatrix},$$

with $\Theta = N^2 x_3^*$ and $\boldsymbol{n} = \boldsymbol{e}_3^*$. When retaining only the terms at leading order of $\varepsilon$, we recover the KBF described by Eq. (2). Obviously, differences between the two base flows can appear for instabilities of order $n \geqslant 2$. In the present study, we only consider Mahalov's base flow for the sake of brevity.

### B. Perturbed system

#### 1. Linearized system in physical space

We substitute the solutions Eq. (9) into the system Eq. (7) and linearize. Linearization is discussed in Sec. I C; it is not readily justified by the fact that the flow disturbances are

very small with respect to the base flow. Thus, we expect our analysis to break down when the disturbances become so large that nonlinear effects become important. The resulting perturbed equations are

$$D_t \boldsymbol{u} = -\boldsymbol{\nabla} p - 2\boldsymbol{\Omega}_p \times \boldsymbol{u} - (\boldsymbol{u}\cdot\boldsymbol{\nabla})\boldsymbol{U} + \vartheta \boldsymbol{n}, \tag{16a}$$

$$D_t \vartheta = -(\boldsymbol{\nabla}\Theta)\cdot\boldsymbol{u} = -N^2\sqrt{1+4\varepsilon^2}\,\boldsymbol{n}\cdot\boldsymbol{u}, \tag{16b}$$

together with the condition that $\boldsymbol{u}$ is solenoidal, i.e., $\boldsymbol{\nabla}\cdot\boldsymbol{u} = 0$. As for the PV linear part, it takes the form

$$\varpi_\kappa = 2\Omega\partial_{x_3}\vartheta - 2\varepsilon N^2(\boldsymbol{\nabla}\times\boldsymbol{u})_1 + N^2(\boldsymbol{\nabla}\times\boldsymbol{u})_3. \tag{17}$$

#### 2. Time-dependent wave vector

The disturbances are expressed in terms of plane waves, for which the direction and the speed of propagation depend on time (see Refs. [20,21], with a extended review in Ref. [22]),

$$[\boldsymbol{u}, p, \vartheta](\boldsymbol{x}, t) = [\hat{\boldsymbol{u}}, \hat{p}, \hat{\vartheta}](\boldsymbol{k}, t)\exp[\mathrm{i}\boldsymbol{x}\cdot\boldsymbol{k}(t)], \tag{18}$$

where $\mathrm{i}^2 = -1$. Accordingly, the material derivative of the fluctuating velocity can be rewritten as

$$D_t\boldsymbol{u} = \left(\partial_t + U_j\frac{\partial}{\partial x_j}\right)[\hat{\boldsymbol{u}}(\boldsymbol{k}, t)\exp\{\mathrm{i}\boldsymbol{x}\cdot\boldsymbol{k}(t)\}],$$

with $U_j = A_{jm}x_m$, so that

$$D_t\boldsymbol{u} = \{\partial_t\hat{\boldsymbol{u}} + \mathrm{i}[(d_t k_j)x_j + A_{jm}k_j x_m]\hat{\boldsymbol{u}}\}\exp[\mathrm{i}\boldsymbol{x}\cdot\boldsymbol{k}(t)],$$

or equivalently,

$$D_t\boldsymbol{u} = \{\partial_t\hat{\boldsymbol{u}} + \mathrm{i}[(d_t\boldsymbol{k} + A^T\boldsymbol{k})\cdot\boldsymbol{x}]\hat{\boldsymbol{u}}\}\exp[\mathrm{i}\boldsymbol{x}\cdot\boldsymbol{k}(t)].$$

To remove the explicit dependence on $\boldsymbol{x}$ in the resulting equations for the Fourier amplitudes $\hat{\boldsymbol{u}}$, $\hat{p}$, $\hat{\vartheta}$, one has to ensure that $\boldsymbol{k}(t)$ varies in time according to the eikonal equation (see Refs. [21,22]),

$$d_t\boldsymbol{k} = -\mathbf{A}^T\cdot\boldsymbol{k}, \tag{19}$$

where $d_t(\cdot) \equiv d(\cdot)/dt$. We substitute the expression of $\mathbf{A}$ given by Eq. (10a) into the eikonal equation, we obtain

$$d_t k_1 = -\Omega k_2, \quad d_t k_2 = \Omega k_1 + 2\varepsilon\Omega k_3, \quad d_t k_3 = 0. \tag{20}$$

This amounts to following characteristic lines of the base flow, although expressed in spectral variables (details in Ref. [15]). We integrate system Eq. (20):

$$k_1 + 2\varepsilon k_3 = (k_{10} + 2\varepsilon k_{30})\cos\tau - k_{20}\sin\tau, \tag{21a}$$

$$k_2 = (k_{10} + 2\varepsilon k_{30})\sin\tau + k_{20}\cos\tau, \tag{21b}$$

$$k_3 = k_{30}, \tag{21c}$$

where $\tau = \Omega t$ being a dimensionless time, $k_{j0}$ $(j = 1, 2, 3)$ denotes the initial wave vector component. For convenience, we introduce the wave number $k_p$ and the angle $\phi$ defined as follows:

$$k_{10} + 2\varepsilon k_{30} = k_p\cos\phi, \quad k_{20} = k_p\sin\phi,$$

so that

$$k_1 + 2\varepsilon k_3 = k_p\cos(\tau+\phi), \tag{22a}$$

$$k_2 = k_p\sin(\tau+\phi), \tag{22b}$$

$$k_3 = k_{30}. \tag{22c}$$

It follows that the wave-vector trajectories are circles with sheared centers (i.e., they are sheared across each other so that the line joining their centers is not now perpendicular to their plane, see Ref. [4]), where $(k_1 + 2\varepsilon k_3)^2 + k_2^2 = k_p^2$ and $k_3 = k_{30}$. For purposes of studying stability, we may set $\phi = 0$. This is easily seen by making the substitution $\Omega t' = \Omega t + \phi$, which eliminates $\phi$ from the equation.

#### 3. Toroidal, poloidal, and buoyancy modes

Substituting the plane waves solution Eq. (18) into the system Eq. (16) and taking into account the eikonal Eq. (19), we obtain

$$d_t\hat{\boldsymbol{u}} = -\mathrm{i}\hat{p}\boldsymbol{k} - 2\boldsymbol{\Omega}_p\times\hat{\boldsymbol{u}} - (\boldsymbol{\nabla}\boldsymbol{U})\cdot\hat{\boldsymbol{u}} + \hat{\vartheta}\boldsymbol{n}, \tag{23a}$$

$$d_t\hat{\vartheta} = -N^2\sqrt{1+4\varepsilon^2}\,\boldsymbol{n}\cdot\hat{\boldsymbol{u}}, \tag{23b}$$

together with $\boldsymbol{k}\cdot\hat{\boldsymbol{u}} = 0$. The use of the later condition allows one to eliminate the Fourier amplitude of fluctuating pressure and to reduce the above fourth order differential system to a third order one.

Alternatively, one may use the following orthonormal basis:

$$\boldsymbol{e}^{(3)} = \frac{\boldsymbol{k}}{k}, \quad \boldsymbol{e}^{(1)} = \frac{\boldsymbol{k}\times\boldsymbol{e}_3}{k_\perp}, \quad \boldsymbol{e}^{(2)} = \boldsymbol{e}^{(3)}\times\boldsymbol{e}^{(1)}, \tag{24}$$

in which the condition $\boldsymbol{k}\cdot\hat{\boldsymbol{u}} = 0$ is satisfied by construction, so that, $\hat{\boldsymbol{u}} = u^{(1)}\boldsymbol{e}^{(1)} + u^{(2)}\boldsymbol{e}^{(2)}$, where

$$u^{(1)} = \frac{k_2}{k_\perp}\hat{u}_1 - \frac{k_1}{k_\perp}\hat{u}_2, \quad u^{(2)} = -\frac{k}{k_\perp}\hat{u}_3, \tag{25}$$

and $k_\perp^2 = k_1^2 + k_2^2$. The two components $u^{(1)}$ and $u^{(2)}$ are respectively called toroidal and poloidal modes (see Ref. [22]). The buoyancy mode $u^{(3)} = \hat{\vartheta}/\Omega$ is re-scaled as a velocity. Therefore, the resulting linear differential system for the modes $(u^{(1)}, u^{(2)}, u^{(3)})$ reads (see Appendix B1)

$$\begin{aligned}
d_\tau u^{(1)} &= \left(2\frac{k_3}{k} + 2\varepsilon\frac{k_1 k}{k_\perp^2}\right)u^{(2)} - \frac{2\varepsilon}{\sqrt{1+4\varepsilon^2}}\frac{k_2}{k_\perp}u^{(3)},\\
d_\tau u^{(2)} &= -\left(2\frac{k_3}{k} + 2\varepsilon\frac{k_1}{k}\frac{k_3^2}{k_\perp^2}\right)u^{(1)} - 2\varepsilon\frac{k_2 k_3}{k^2}u^{(2)}\\
&\quad - \frac{1}{\sqrt{1+4\varepsilon^2}}\left(\frac{k_\perp}{k} + 2\varepsilon\frac{k_1}{k}\frac{k_3}{k_\perp}\right)u^{(3)},\\
d_\tau u^{(3)} &= 2\varepsilon\mathcal{N}^2\frac{k_2}{k_\perp}u^{(1)} + \mathcal{N}^2\left(\frac{k_\perp}{k} + 2\varepsilon\frac{k_1}{k}\frac{k_3}{k_\perp}\right)u^{(2)},
\end{aligned} \tag{26}$$

or equivalently, in a matrix form, by introducing the fundamental matrix $\boldsymbol{\Phi}_3(\tau)$ with $\boldsymbol{\Phi}_3(0)$ being the unit matrix $\mathbf{I}_3$,

$$d_\tau\boldsymbol{\Phi}_3 = \mathbf{D}_3\cdot\boldsymbol{\Phi}_3. \tag{27}$$

Note that the determinant $|\boldsymbol{\Phi}_3|$ of the matrix $\boldsymbol{\Phi}_3$, takes the form

$$|\boldsymbol{\Phi}_3| = \exp\left[\int_0^\tau \mathrm{Tr}\,\mathbf{D}_3(s)ds\right] = \frac{k(0)}{k(\tau)},$$

where (Tr $\mathbf{D}$) denotes the trace of the matrix $\mathbf{D}$. Therefore, $|\boldsymbol{\Phi}_3|$ reduces to unity at $\tau = 2\pi$ since the wave vector $\boldsymbol{k}$ is $2\pi-$ periodic. Consequently, the product of the eigenvalues of the monodromy matrix $\mathbf{M}_3 = \boldsymbol{\Phi}_3(2\pi)$ is unity.

By using a fourth-order Runge-Kutta-Gill method we have determined the matrix $\mathbf{M}_3$ and its eigenvalues (called Floquet multipliers) for several values of the parameters $\varepsilon$, $\mathcal{N}$ and $\mu$ (see below). The numerical results indicate that one Floquet multiplier $\lambda_3$ (say) is unity, and hence, the others being complex conjugates of each other or real reciprocals since $|\mathbf{M}_3| = 1$. More details on the stability of system Eq. (26) is given in the next section.

For system Eq. (26), there are three dimensionless parameters, namely,

$$\varepsilon = \Omega_p/\Omega, \quad \mathcal{N} = N/\Omega, \quad \text{and} \quad \mu = k_3/\sqrt{k_p^2 + k_3^2}, \tag{28}$$

where $\mathcal{N}$ measures the strength of stratification to rotation. Recall that both the wave numbers $k_3$ and $k_p$ are time-independent. Without precession ($\varepsilon = 0$), the angle $\cos^{-1}(\mu)$ is the angle between the wave vector and the solid-body rotation axis. Note that the mode with $k_p = \sqrt{(k_1 + 2\varepsilon k_3)^2 + k_2^2} = 0$ is stable provided $\varepsilon < 0.50$ (see Appendix B2).

### C. Reduced Floquet systems

Thanks to Eq. (17), the Floquet system Eq. (26) can be further reduced. Indeed, the fact that PV is a Lagrangian invariant [see Eq. (17)] allows one to express the buoyancy mode in terms of the toroidal and poloidal ones if $k_3 \neq 0$, or to express the toroidal mode in function of the poloidal one if $k_3 = 0$,

$$2k_3 u^{(3)} - \mathcal{N}^2\left[k_\perp\left(1 + 2\varepsilon\frac{k_1 k_3}{k_\perp^2}\right)u^{(1)} - 2\varepsilon k_2\frac{k}{k_\perp}u^{(2)}\right] = \frac{\hat{\varpi}_\kappa}{\Omega}, \tag{29}$$

where $\hat{\varpi}$ is the spectral counterpart of PV. Consequently, we study separately the stability of the two cases $k_3 = 0$ and $k_3 \neq 0$.

In the case where $k_3 \neq 0$, we deduce from Eq. (29) the expression of $u^{(3)}$ in terms of $u^{(1)}$ and $u^{(2)}$,

$$u^{(3)} = \frac{\mathcal{N}^2}{2}\left(\frac{k_\perp}{k_3} + 2\varepsilon\frac{k_1}{k_\perp}\right)u^{(1)} - \varepsilon\mathcal{N}^2\frac{k}{k_3}\frac{k_2}{k_\perp}u^{(2)} + \frac{\hat{\varpi}_\kappa}{k_3\Omega},$$

and we substitute it into the first two equations of system (26), we obtain the following reduced two-dimensional inhomogeneous system,

$$d_\tau\hat{\boldsymbol{u}} = \mathbf{D}\cdot\hat{\boldsymbol{u}} + \hat{\boldsymbol{\varphi}}, \tag{30}$$

where

$$D_{11} = -\frac{\varepsilon\mathcal{N}^2}{\sqrt{1+4\varepsilon^2}}\left(\frac{k_2}{k_3} + 2\varepsilon\frac{k_1 k_2}{k_\perp^2}\right), \tag{31a}$$

$$D_{12} = 2\frac{k_3}{k} + 2\varepsilon\frac{k_1 k}{k_\perp^2} + 2\varepsilon^2\mathcal{N}^2\frac{k}{k_3}\frac{k_2^2}{k_\perp^2}, \tag{31b}$$

$$D_{21} = -2\frac{k_3}{k} - 2\varepsilon\frac{k_1}{k}\frac{k_3^2}{k_\perp^2} - \frac{\mathcal{N}^2}{2\sqrt{1+4\varepsilon^2}}\left(\frac{k_\perp^2}{k_3 k} + 4\varepsilon\frac{k_1}{k}\right), \tag{31c}$$

$$D_{22} = -D_{11} - 2\varepsilon\frac{k_2 k_3}{k^2} = -D_{11} - \frac{1}{k}d_\tau k. \tag{31d}$$

The inhomogeneous term in Eq. (30) takes the form

$$\varphi^{(1)} = -\frac{2\varepsilon}{\sqrt{1+4\varepsilon^2}}\frac{k_2}{k_\perp}\frac{\hat{\varpi}_\kappa}{k_3\Omega}, \tag{32a}$$

$$\varphi^{(2)} = -\frac{1}{\sqrt{1+4\varepsilon^2}}\left(\frac{k_\perp}{k} + 2\varepsilon\frac{k_1}{k}\frac{k_3}{k_\perp}\right)\frac{\hat{\varpi}_\kappa}{k_3\Omega}, \tag{32b}$$

and it can be seen as a time-varying forcing excitation. The linear system Eq. (30) has the properties $\mathbf{D}(\tau + T) = \mathbf{D}(\tau)$ and $\hat{\boldsymbol{\varphi}}(\tau + T) = \hat{\boldsymbol{\varphi}}(\tau)$, where $T = 2\pi$ is the period common to both the matrix $\mathbf{D}$ and the vector $\hat{\boldsymbol{\varphi}}$. Floquet theory does not address stability of the inhomogeneous system described by Eq. (30), where the "forcing excitation" $\hat{\boldsymbol{\varphi}}(\tau)$ is present. However, the $T$-periodic nature of $\hat{\boldsymbol{\varphi}}(\tau)$ allows an extension to the theory (see Slane and Tragesser [46]). Following the study of Slane and Tragesser [46], it is shown that the basic behavior of the homogeneous system,

$$d_\tau\hat{\boldsymbol{u}} = \mathbf{D}\cdot\hat{\boldsymbol{u}}, \tag{33}$$

does not change with the addition of the term $\hat{\boldsymbol{\varphi}}(\tau)$. In other words, for purposes of studying stability, one may set $\hat{\varpi}_\kappa = 0$, so that $\hat{\boldsymbol{\varphi}} = \mathbf{0}$.

We denote by $\boldsymbol{\Phi}(\tau)$ any fundamental matrix solution of the homogeneous system Eq. (33), where $\boldsymbol{\Phi}(0) = \mathbf{I}_2$. According to Floquet-Lyapunov theorem, $\boldsymbol{\Phi}$ is expressible in the form (see, e.g., Ref. [47]),

$$\boldsymbol{\Phi}(\tau) = \mathbf{F}(\tau)\exp(\mathbf{K}\tau), \tag{34}$$

where $\mathbf{F}(\tau)$ is a nonsingular continuous $2\pi$-periodic $2\times 2$ matrix-function (whose derivative is an integrable piecewise-continuous function) and $\mathbf{K}$ is a constant matrix. Also the determinant of $\boldsymbol{\Phi}$ is unity at $\tau = 2\pi$, $|\boldsymbol{\Phi}(2\pi)| = 1$. It follows that whenever $\lambda$ is an eigenvalue of the monodromy matrix, $\mathbf{M} = \boldsymbol{\Phi}(2\pi)$, so also are its inverse $\lambda^{-1}$ and its complex conjugate $\lambda^*$ (see also Ref. [44]).

Consequently, in the stable case, eigenvalues of $\mathbf{M}$ lie on the unit circle: each one of two multipliers is not identically one, but has both real and imaginary parts with magnitude equal to one, and is semisimple, $\lambda_{1,2} = \lambda_{1r} \pm \mathrm{i}\lambda_{1i}$ with $\lambda_{1r}^2 + \lambda_{1i}^2 = 1$. In that case, the solution to the inhomogeneous system Eq. (30) after $n$ time periods, where $n$ is an integer, takes the form

$$\hat{\mathbf{u}}(2n\pi) = \mathbf{M}^n\hat{\mathbf{u}}(0) + \left[\sum_{\ell=1}^{n}\mathbf{M}^\ell\right]\int_0^{2\pi}\boldsymbol{\Phi}(\tau)^{-1}\hat{\boldsymbol{\varphi}}(\tau)d\tau, \tag{35}$$

and is bounded as $n$ increases to infinity [46].

In counterpart, if, as parameters change, an eigenvalue of $\mathbf{M}$ is at the onset of instability, then it must have multiplicity two, i.e., $\lambda_1 = \lambda_2 = \pm 1$. Thus a necessary condition for the onset of instability of system Eq. (33) is a resonance where two Floquet Floquet characteristic exponents, $\sigma_{1,2} = (\log\lambda_{1,2}/(2\pi)$, coincide (see Ref. [44]). There is instability whenever $\Re\sigma_{1,2} > 0$ that is, whenever

$$|\mathrm{Tr}\,\mathbf{M}| = |\lambda_1 + \lambda_2| = \left|\lambda_1 + \lambda_1^{-1}\right| > 2. \tag{36}$$

For these two cases (i.e., when $\lambda_1 = \lambda_2 = \pm 1$ or $|\lambda_1 + \lambda_1^{-1}| > 2$), the inhomogeneous solution $\hat{\mathbf{u}}(2n\pi)$ is unbounded as as $n$ increases to infinity [46].

Accordingly, for purposes of studying stability, one may set $\hat{\varpi}_\kappa = 0$. The same conclusion can be drawn from computations. Indeed, for a given of the triplet $(\mu, \varepsilon, \mathcal{N})$, the systems Eqs. (26) and (33) yields the same regions of instability.

## III. RESONANT INERTIA-GRAVITY WAVES

In this section, we discuss the resonant cases of inertia-gravity waves which characterize the onset of linear instability. At $\varepsilon = 0$, the matrix $\mathbf{D}$ in system Eq. (30) reduces to

$$\mathbf{D_0} \equiv \mathbf{D}(\varepsilon = 0) = \begin{bmatrix} 0 & 2\mu \\ -2\mu - \frac{1}{2}\mathcal{N}^2\mu^{-1}(1-\mu^2) & 0 \end{bmatrix} \tag{37}$$

and admits two distinct eigenvalues $\sigma_{1,2}$ associated to the two frequencies, $\omega_{1,2} = -\mathrm{i}\Omega\sigma_{1,2}$, of inertia-gravity waves,

$$\omega_{1,2} = \pm\sqrt{\omega_r^2 + \omega_g^2} = \pm\Omega\sqrt{4\mu^2 + \mathcal{N}^2(1-\mu^2)}, \tag{38}$$

where

$$\omega_r = \pm 2\Omega\cos(\boldsymbol{\Omega}, \boldsymbol{k}) = \pm 2\Omega\mu, \tag{39a}$$

$$\omega_g = \pm N\sin(\boldsymbol{n}, \boldsymbol{k}) = \pm N\sqrt{1-\mu^2} \tag{39b}$$

are the frequencies of inertial and internal gravity waves, respectively.

Disturbances induced by the unstratified flow with circular streamlines (so that, $\varepsilon = 0$ and $N = 0$), are inertial waves with frequency $\omega_r$. With additional stable vertical stratification ($N^2 > 0$), there are inertia-gravity waves propagating with frequency $\omega_{1,2} = \pm\sqrt{\omega_r^2 + \omega_g^2}$.

The resonant cases of inertia-gravity waves are those parameter values $(\mu, \mathcal{N})$ such that $\omega_1 - \omega_2 = n\Omega$, where $n$ is an integer. Since $\omega_2 = -\omega_1$ [see Eq. (38)], the resonant cases are then characterized by

$$\Omega^{-2}\omega_1^2 = (4 - \mathcal{N}^2)\mu^2 + \mathcal{N}^2 = \frac{n^2}{4}. \tag{40}$$

The condition Eq. (40) for resonance readily extends the one by Bayly [20], foreshadowed in the Cambon's thesis (1982, details in Ref. [22]), for basic elliptical flow instability. Note that $\pi/\Omega$ is the typical time (period) for a wave packet to run the closed elliptical streamline, in the limit of vanishing, but nonzero, $\varepsilon$; in the same limit, this period characterizes the periodic alignment of the fluctuating vorticity with the mean (weak) strain, as $2\pi/\omega$. The condition can be written $4\Omega\mu = n\Omega$ from the seminal study [20], that immediately yielded $\mu = n/4$, giving the origin of angle-dependent instability tongues at vanishing $\varepsilon$. The main (harmonic instability) case of $n = \pm 2$, $\mu = \pm\frac{1}{2}$ was the easiest to display, numerically or experimentally.

Because $\omega_1^2(-\mu) = \omega_1^2(\mu)$ and $\omega_1^2(-n) = \omega_1^2(n)$, we only consider, without a loss of generality, $0 \leqslant \mu \leqslant 1$ and $n \in \mathbb{N}$. Relation Eq. (40) implies that

$$\begin{array}{lll} 2\mathcal{N} \leqslant n < 4 & \text{if} & 0 < \mathcal{N} < 2, \\ n = 4 & \text{if} & \mathcal{N} = 2 \text{ or if } \mu^2 = 1, \\ 4 < n \leqslant 2\mathcal{N} & \text{if} & 2 < \mathcal{N}. \end{array}$$

Therefore, the resonant cases of order $n = 1$ exist for $\mathcal{N} \leqslant 0.5$, those of order $n = 2$ exist for $\mathcal{N} \leqslant 1$, while those of order $n = 3$ exist for $\mathcal{N} \leqslant 1.5$, implying that

$$\mu = \frac{1}{2}\sqrt{\frac{n^2 - 4\mathcal{N}^2}{4 - \mathcal{N}^2}} \leqslant \frac{n}{4}, \quad n = 1, 2, 3, \quad \text{and} \quad \mathcal{N} \leqslant \frac{3}{2}. \tag{41}$$

Thus, for $n = 1$ (respectively, $n = 2$ or $n = 3$) the ratio $\mu$ changes from 0.25 (respectively, 0.5 or 0.75) at $\mathcal{N} = 0$ to 0 as $\mathcal{N} = 0.5$ (respectively, $\mathcal{N} = 1$ or $\mathcal{N} = 1.5$). Resonant cases of order $n = 4$ exist for all values of $\mathcal{N}$ implying that $0 \leqslant \mu \leqslant 1$ if $\mathcal{N} = 2$ or $\mu = 1$ otherwise (see Fig. 3).

When $1.5 < \mathcal{N} \leqslant 2.5$ there are only resonant cases of order $n = 4$. In counterpart, when $\mathcal{N} > 2.5$, only resonant cases of order greater than or equal to 4 exist, implying that $\mu = 1$ for $n = 4$, or

$$\mu = \frac{1}{2}\sqrt{\frac{4\mathcal{N}^2 - n^2}{\mathcal{N}^2 - 4}} < 1 \tag{42}$$

for $4 < n \leqslant 2\mathcal{N}$. Figure 3 shows the variation of $\mathcal{N}$ versus $\mu$. For fixed $\mathcal{N}$, the intersect of the horizontal straight line with the curve $\mathcal{N}(\mu, n)$ determines the resonant cases (at least, resonant cases of order $n = 4$ exist).

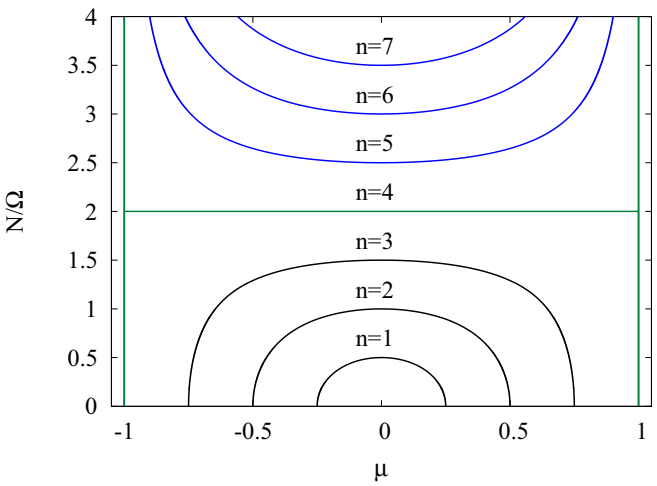


FIG. 3. The first seven resonant cases of inertia-gravity waves according to the dispersion relation Eq. (40). For fixed $\mathcal{N}$, the intersection of the horizontal straight line with the curve $\mathcal{N}(\mu, n)$ determines the resonant cases.

Note that in the purely stratified case (i.e., $\Omega = 0$) the modes with $\mu = \pm 1$ (so that $\omega_g = 0$) are called "slow" modes. In the case with $N = 0$ (the purely rotating flow), the "slow" modes correspond to two-dimensional modes with $\mu = 0$. For $N = 2\Omega$ the group velocity

$$\boldsymbol{v}_g = \nabla_{\boldsymbol{k}}\omega_1(\boldsymbol{k}) = \frac{(4\Omega^2 - N^2)}{\omega k^4}[\boldsymbol{k} \times (k_3\boldsymbol{e}_3 \times \boldsymbol{k})]$$

is zero, signifying that, in the linear limit, the wave energy does not propagate. We also note that the regime of rapid rotation and strong stratification with $\mathcal{N} \equiv N/\Omega > 2$ is most relevant to the atmosphere and ocean (see Ref. [48]) and for $\mathcal{N} < 2$ convective columns are likely to form. Although the present linear analysis concerns only the dynamics of a single mode $\boldsymbol{k}$ which cannot interact with itself, it is instructive to note that, nonlinear resonant triad interactions, which require

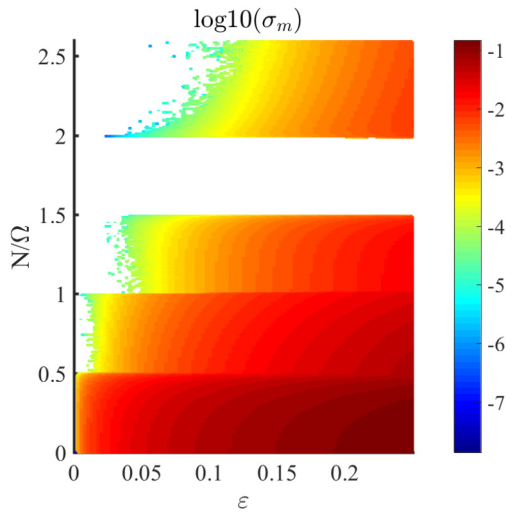


FIG. 4. Inviscid instabilities on the $(\varepsilon, \mathcal{N} = N/\Omega)$ plane for the stratified precessing flow. Let $\sigma_{mn}$ with $n = 1, 2, 3, 4$ be the maximal growth rate of the instability of order $n$ over $0 \leqslant \mu \leqslant 1$). The figure displays $\max(\sigma_{m1}, \sigma_{m2}, \sigma_{m3}, \sigma_{m4})$ determined numerically as a function of the parameters $\varepsilon$ and $\mathcal{N}$. The white band between $N = 1.5$ and $\mathcal{N} = 2$ corresponds to the case where there is no instability, in agreement with the analysis presented in Sec. III. In counterpart, for $0.5 < \mathcal{N} < 1.5$ or $2 \leqslant \mathcal{N} \leqslant 2.6$, the white areas correspond to very small values ($< 10^{-8}$) of the maximal growth rate.

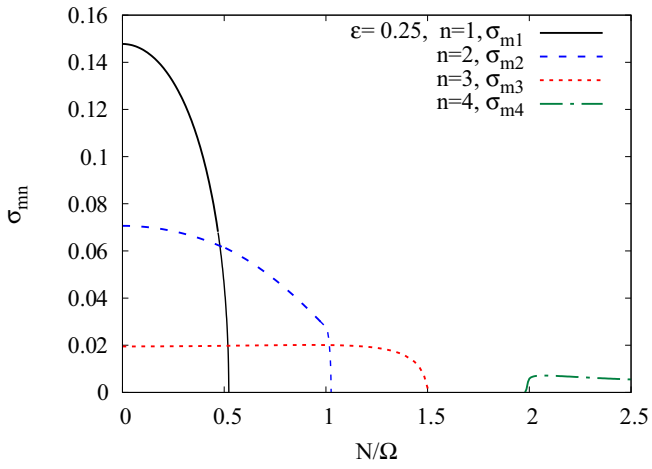


FIG. 5. Destabilizing resonant cases of order $n = 1, 2, 3, 4$. The figure shows the maximal growth rate ($\sigma_{mn}$) of each one of these four unstable cases versus $\mathcal{N}$ for $\varepsilon = 0.25$.

that the interacting modes $\boldsymbol{k}$, $\boldsymbol{p}$, and $\boldsymbol{q}$ form a triangle and $\omega_1(\boldsymbol{k}) + \omega_1(\boldsymbol{p}) + \omega_1(\boldsymbol{q}) = 0$ where $\omega$ is given in Eq. (38), cannot occur for $1 \leqslant \mathcal{N} \leqslant 4$ (see Ref. [49]). For the later range ($1 \leqslant \mathcal{N} \leqslant 4$), quasigeostrophic (QG) motions are expected to dominate the dynamics of rotating stratified turbulence, while the strength of the waves is weaker (see, e.g., Refs. [50,51]).

## IV. STABILITY ANALYSIS

In this section, we investigate the destabilizing resonant cases of precessing inertia-gravity waves. Our analysis is based on numerical computations and on an asymptotic analysis to leading order in $\varepsilon$. The asymptotic analysis to leading order in $\varepsilon$ is performed by extending analytical techniques developed by Lebovitz and Zweibel [44]. For the sake of clarity, all the asymptotic calculations are reported in Appendix C. Here we only state the results.

In Fig. 4, we show the continuous variation of the dominant inviscid instability. Let $\sigma_{mn}$ with $n = 1, 2, 3, 4$ be the maximal growth rate of the instability of order $n$. The figure displays $\max(\sigma_{m1}, \sigma_{m2}, \sigma_{m3}, \sigma_{m4})$ determined numerically as a function of the parameters $\varepsilon$ and $\mathcal{N}$. The grid consists of 101 points evenly distributed in the interval $0 \leqslant \varepsilon \leqslant 0.25$ and 361 points evenly distributed in the interval $0 \leqslant \mathcal{N} \leqslant 2.6$). The fact that Fig. 4 is divided into horizontal bands can be explained as follows.

In the range $0 < \mathcal{N} < 0.5$, the instabilities of order $n = 1, 2, 3$ exist but it is the subharmonic instability ($n = 1$) which is the strongest: its maximum growth rate is strictly greater than that of the other two instabilities as shown in Fig. 5, so that, $\max_{n=1,2,3}(\sigma_{nm}) = \sigma_{m1}$. Figure 5 shows $\sigma_{mn}$ with $n = 1, 2, 3, 4$ versus $\mathcal{N}$ for $\varepsilon = 0.25$.

In the range $0.5 \leqslant \mathcal{N} \leqslant 1$ the subharmonic instability is suppressed by the stratification and only the instabilities of order $n = 2, 3$ exist, but the growth rate, $\sigma_{n2}$ of the harmonic instability ($n = 2$) is strictly greater than that of the instability of order $n = 3$ (see Fig. 5), so that, $\max_{n=1,2,3}(\sigma_{nm}) = \sigma_{m2}$.

In the range $1 < \mathcal{N} < 1.5$, the harmonic instability ($n = 2$) is also suppressed and only the instability of order $n = 3$ exists, so that, $\max_{n=1,2,3}(\sigma_{nm}) = \sigma_{m3}$.

The white band corresponds to the case where $1.5 \leqslant \mathcal{N} < 2$ for which there is no instability, in agreement with the analysis presented in Sec. III which indicates that there is no resonant cases of inertia-gravity waves for $1.5 \leqslant \mathcal{N} < 2$.

The instability occurring for $2 \leqslant \mathcal{N} \leqslant 2.6$, is weaker than those observed for $0 \leqslant \mathcal{N} \leqslant 1.5$. For convenience, we denote by $\mathcal{D}_1, ..., \mathcal{D}_5$ the five domains of Fig. 4: those for which $0 \leqslant \mathcal{N} \leqslant 0.5$, $0.5 \leqslant \mathcal{N} \leqslant 1$, $1 \leqslant \mathcal{N} \leqslant 1.5$, $1.5 \leqslant \mathcal{N} \leqslant 2$, and $2 \leqslant \mathcal{N} \leqslant 2.6$, respectively.

### A. Subharmonic instability

The results yielded by the asymptotic analysis to leading order in $\varepsilon$ (see Appendix C) allows us to characterize the effects of stable stratification on the subharmonic instability (i.e., the one resulting from the resonant case of order $n = 1$). The asymptotic analysis, as well as numerical computations, indicate that the precessional subharmonic instability occurs for $0 \leqslant \mathcal{N} < 0.5$ and gets suppressed at $\mathcal{N} = 0.5$.

According to the asymptotic analysis, for a given value of $\mathcal{N}$, the region in the $(\mu, \varepsilon)$ plane where the subharmonic instability occurs is typically a wedge with apex at a point $(0, \mu_0)$ such that [see Eq. (41) with $n = 1$]

$$\mu_0 = \frac{1}{2}\sqrt{\frac{1 - 4\mathcal{N}^2}{4 - \mathcal{N}^2}} \leqslant \frac{1}{4}, \tag{43}$$

and boundaries

$$\mu = \mu_0 + \nu_\pm \varepsilon, \tag{44}$$

where the slopes $\nu_\pm$ are [see Eq. (C23) in Appendix C3]

$$\nu_\pm = \pm\frac{5\sqrt{15}}{64}\left(1 - \frac{\mathcal{N}^2}{4}\right)^{-\frac{3}{2}}. \tag{45}$$

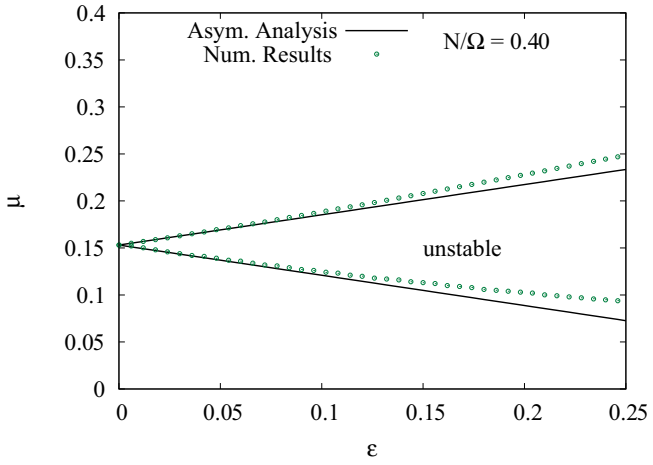


FIG. 6. Destabilizing resonant case of order $n = 1$ (i.e., the subharmonic instability). The figure shows the instability band in the $(\varepsilon, \mu)$ plane for $\mathcal{N} = 0.4$. The lines correspond to the results yielded by the asymptotic analysis [see Eq. (44)]. Symbols represent the numerical results.

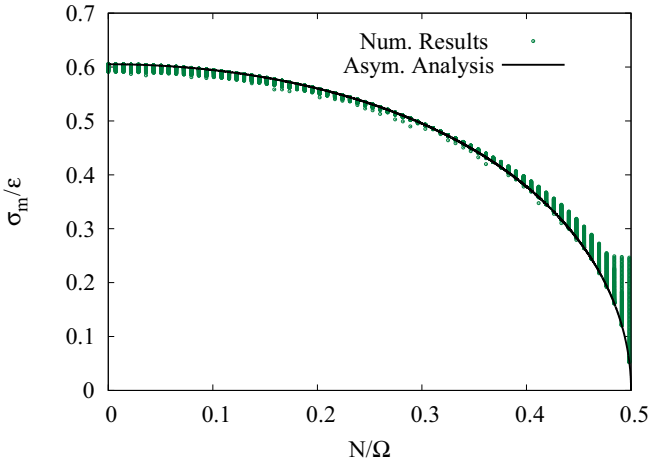


FIG. 7. Destabilizing resonant case of order $n = 1$. The figure shows the maximal growth rate $\sigma_{m1}$ normalized by $\varepsilon$ versus $\mathcal{N} \equiv N/\Omega$. The line corresponds to Eq. (46) yielded by the asymptotic analysis. Symbols represent all the points (7070 points) of the domain $0 \leqslant \varepsilon \leqslant 0.25$ and $0 \leqslant \mathcal{N} \leqslant 0.5$ in Fig. 4.

We no longer need the designation $\mu_0$ and, hereinafter, use the symbol $\mu$ in its place, except in Appendix C.

The subharmonic instability has a bandwidth $(\nu_+ - \nu_-)\varepsilon$ that is, for given $\varepsilon$ and $\mathcal{N}$, the length of the $\mu$ interval for which the unperturbed configuration is unstable (see Ref. [44]). The maximal growth rate $\sigma_{m1}$ of the subharmonic instability is [see Eqs. (C22) and (C23) in Appendix C3]

$$\sigma_{m1} = \varepsilon \frac{5\sqrt{15}}{8} \frac{\sqrt{1 - 4\mathcal{N}^2}}{(4 - \mathcal{N}^2)}. \tag{46}$$

Without stratification, $\mathcal{N} = 0$, the subharmonic instability band in the $(\mu, \varepsilon)$ plane emanates from the point $(\mu = 0.25, 0)$ with maximal growth rate $\sigma_{m1} = (5\sqrt{15}/32)\varepsilon$ as suggested by Eq. (46) (see also Refs. [4,15]).

When stratification is not zero, the point of the $\mu$ axis at which occurs the subharmonic instability moves to the left as $\mathcal{N}(< 0.5)$ increases, so as it reaches to the point (0,0) at $\mathcal{N} = 0.5$. Figure 6 shows the instability band in the $(\varepsilon, \mu)$ plane for $\mathcal{N} = 0.4$ As it can be seen, there is an expected agreement between Eqs. (44) and (45), especially for $\varepsilon < 0.2$. We note that the the bandwidth of the subharmonic instability does not substantially change when $\mathcal{N}$ increases ($0 \leqslant \mathcal{N} < 0.5$). For this, here we only show the region of the subharmonic instability in the $(\varepsilon, \mu)$ plane (see Fig. 6) determined at $\mathcal{N} = 0.4$.

In counterpart, the maximal growth rate $\sigma_{m1}$ is drastically reduced as $\mathcal{N}$ increases, so as $\sigma_{m1} = 0$ at $\mathcal{N} = 0.5$. In other words, stable stratification acts in such a way as to make the subharmonic instability less efficient so as it disappears when $\mathcal{N} \geqslant 0.5$. In Fig. 7, we plot the maximal growth rate $\sigma_{m1}$ normalized by $\varepsilon$ versus $\mathcal{N} \leqslant 0.5$. The numerical data reported in Fig. 7 correspond to all the (7070) points of the domain $0 \leqslant \varepsilon \leqslant 0.25$ and $0 \leqslant \mathcal{N} \leqslant 0.5$ in Fig. 4. We observe that the numerical results well follows the relation Eq. (46) except near $\mathcal{N} = 0.5$. This is due to the fact that, near $\mathcal{N} = 0.5$, the subharmonic instability becomes weaker than the harmonic instability (i.e., the one corresponding to the destabilizing resonant case of order $n = 2$) as explained as follows. With the help of the dispersion relation [see Eqs. (41) and (42)], in the sense that it allows us to localize the point of $\mu$ axis at which emanates the instability, we have determined numerically the maximal growth rate $\sigma_{mn}$ of each of instabilities of order $n = 1$–4.

The numerical results indicate that, for $0 < \mathcal{N} \lesssim 0.48$, $\sigma_{n1}$ remains greater than $\sigma_{n2}$, signifying that the subharmonic instability is the strongest. However, near $\mathcal{N} = 0.5$, $\sigma_{n2}$ becomes greater than $\sigma_{n1}$ and the instability of order $n = 2$ becomes the strongest, as shown by Fig. 5.

### B. Destabilizing resonant cases of order $n = 2, 3, 4, 5$

The investigation of the destabilizing resonant cases of order $n > 1$ is based on the numerical computations performed for 101 (respectively, 361) values evenly distributed in the interval $0 \leqslant \varepsilon \leqslant 0.25$ (respectively, $0 \leqslant \mathcal{N} \leqslant 2.6$), as already indicated. This implies that $n = 2, 3, 4, 5$ according to relations Eqs. (41) and (42) given in the Sec. III. Note that the destabilizing resonant cases of order $n > 5$, which can occur for $\mathcal{N} \geqslant 3$, are likely to be weak and difficult to spot.

The instability resulting from the resonant case of order $n = 2$ (sometimes called harmonic instability) exists for $0 \leqslant \mathcal{N} \leqslant 1$. In the range $0 \leqslant \mathcal{N} \lesssim 0.48$, the subharmonic instability remains weaker than the subharmonic one, while in the range $0 \leqslant \mathcal{N} \leqslant 0.5$ it becomes the strongest. The point of the $\mu$ axis at which emanates this instability is given by Eq. (41) with $n = 2$ : without stratification ($\mathcal{N} = 0$), it emanates from $\mu = 0.5$, and at $\mathcal{N} = 1$ it emanates from $\mu = 0$. Recall that, at $k_3 = 0$ so that $\mu = 0$, the frequency of inertia-gravity waves is equal to the Brunt-Väisälä frequency $N$. In that case ($k_3 = 0$), the resonant case of order $n = 2$ is unstable near $\mathcal{N} = 1$ (see the next section)

In Fig. 8, we plot the maximal growth rate of this instability $\sigma_{m2}$ normalized by $\varepsilon^2$ versus $\mathcal{N}$. The numerical data reported in Fig. 8 correspond to all the points of the domain $0 \leqslant \varepsilon \leqslant 0.25$ and $0.5 \leqslant \mathcal{N} \leqslant 1.03$ in Fig. 4. As it can be

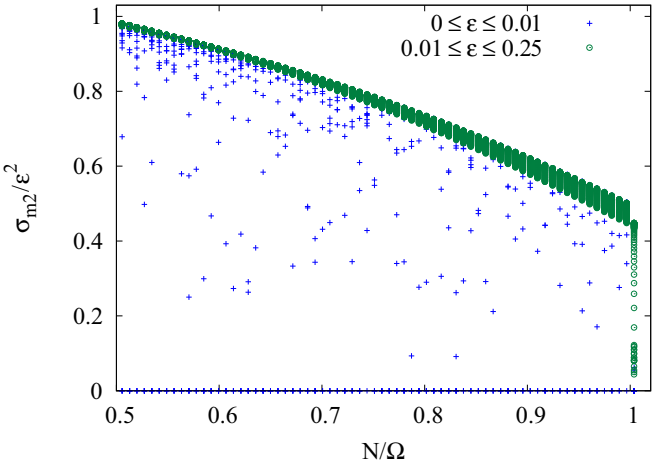


FIG. 8. Destabilizing resonant cases of order $n = 2$ (i.e., harmonic instability). The figure shows the maximal growth rate ($\sigma_{m2}$) of the instability normalized by $\varepsilon^2$ versus $\mathcal{N}$ for $0 \leqslant \varepsilon \leqslant 0.25$.

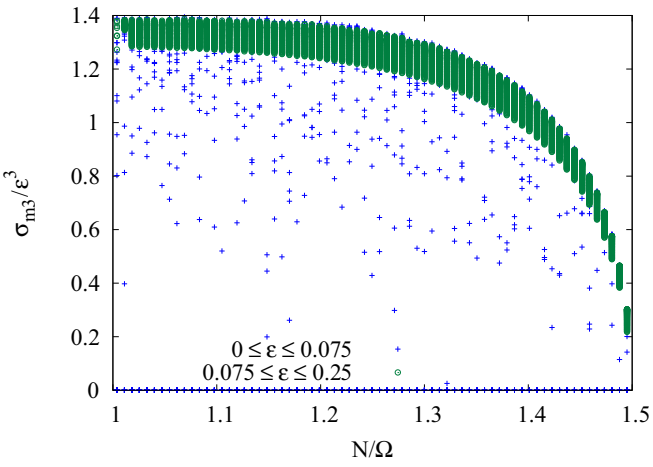


FIG. 9. Destabilizing resonant cases of order $n = 3$. The figure shows the maximal growth rate ($\sigma_{m3}$) of the instability normalized by $\varepsilon^3$ versus $\mathcal{N}$ for $0 \leqslant \varepsilon \leqslant 0.25$.

seen, some of the points for which $0 \leqslant \varepsilon \precsim 0.01$ are not correlated and show an important disparity. They correspond to the white subdomain (for which the maximal growth rate is very weak) of the domain $\mathcal{D}_2$ in Fig. 4. The behavior of the correlated points indicates that $\sigma_{m2}/\varepsilon^2 \approx 1$ at $\mathcal{N} = 0.5$ and decreases as $\mathcal{N}$ increases so as, it takes the value $\sigma_{m2}/\varepsilon = 0.5$ at $\mathcal{N} = 1$, and after, it decreases very quickly and reach zero, $\sigma_{m2}/\varepsilon^2 \approx 0$, at $\mathcal{N} \approx 1.03$. The behavior of $\sigma_{m2}/\varepsilon^2$ near $\mathcal{N} = 1$ could be due to the fact that, at $k_3 = 0$, the resonant case of order $n = 2$ is destabilizing where its maximal growth rate is found as $\sigma_{m2}/\varepsilon^2 = 0.5$ (see the next section). The destabilizing resonant case of order $n = 2$ gets suppressed by stable stratification at $\mathcal{N} \approx 1.03$ and completely disappears beyond this threshold.

In the range $1 < \mathcal{N} < 1.5$, only the instability of order $n = 3$ survives to the effect of stable stratification. Without stratification, this instability emanates from the point $\mu = 0.75$ of the $\mu$ axis. In the presence of stratification, the point from which emanates this instability moves to the left to reach to $\mu = 0$ at $\mathcal{N} = 1.5$ [see Eq. (41)].

In Fig. 9, we plot $\sigma_{m3}/\varepsilon^3$ versus $1 \leqslant \mathcal{N} \leqslant 1.5$. The numerical data reported in Fig. 9 correspond to all the points of domain 3 of Fig. 4. It appears that some points among those for which $0 \leqslant \varepsilon \precsim 0.075$ are not correlated and are very scattered in the diagram $(\mathcal{N}, \sigma_{m3}/\varepsilon^3)$, and correspond to the white subdomain of the domain 3 of Fig. 4. The points for $0.075 \precsim \varepsilon \leqslant 0.25$ seem to be correlated. The behavior of these 'correlated' points indicates that $\sigma_{m3}/\varepsilon^3 \approx 1.3$ at $\mathcal{N} \approx 1$, and decreases as $\mathcal{N}$ increases to reach zero at $\mathcal{N} = 1.5$. At $k_3 = 0$, the resonant case of order $n = 3$, which occurs for $\mathcal{N} = 1.5$ [see Eq. (41)], is not destabilizing (see the next section). Therefore, the destabilizing resonant case of order $n = 3$ gets suppressed at $\mathcal{N} = 1.5$ and does not exist beyond this threshold ($\mathcal{N} = 1.5$).

In the range $1.5 \leqslant \mathcal{N} < 2$, there are no resonant cases of inertia-gravity waves, as shown in Sec. III. In addition, computations do not reveal the presence of any instability in this range which corresponds to the white domain (domain 4) of Fig. 4.

For $\mathcal{N} = 2$, all the points of the interval $0 \leqslant \mu \leqslant 1$ are resonant cases of order $n = 4$, as indicated earlier. However, the present numerical computations indicate that they are not all destabilizing. Indeed, only three narrow bands of instability are detected: they emanate from $\mu = 0$, $\mu \approx 0.38$ and $\mu = 1$, respectively (see Fig. 10). The later one is much narrower though visible on the scale of the figure.

Numerical computations reveal that, for any given value of $\mathcal{N}$ in the range $2 < \mathcal{N} < 2.5$, it exists an instability band that emanates from $\mu = 1$ and remains narrow with a weak growth rate, especially for $0 \leqslant \varepsilon \precsim 0.15$ (see domain 5 of Fig. 4). In Fig. 11, we plot the maximal growth rate $\sigma_{m4}$ normalized by $\varepsilon^4$ versus $\mathcal{N}$. As it can be seen, the points for which $0 \leqslant \varepsilon \leqslant 0.15$ are scattered and many of them are characterized by a very small growth rate (see also Fig. 4). For $0.15 \leqslant \varepsilon \leqslant 0.25$, one has $1 \precsim \sigma_{m4}/\varepsilon^4 \precsim 1$.

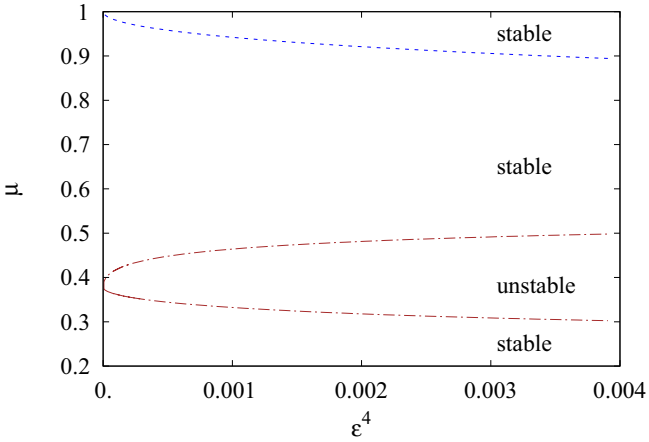


FIG. 10. Destabilizing resonant case of order $n = 4$. The figure shows the regions of instability in the $(\varepsilon^4, \mu)$ plane for $\mathcal{N} = 2$. The instability band emanating from the point $(0, \mu = 1)$ is much narrower though visible on the scale of the figure. The other instability band emanates from the point $(0, \mu = 0.38)$ and its maximal growth rate is about $\sigma_{m4} \approx 1.8\varepsilon^4$.

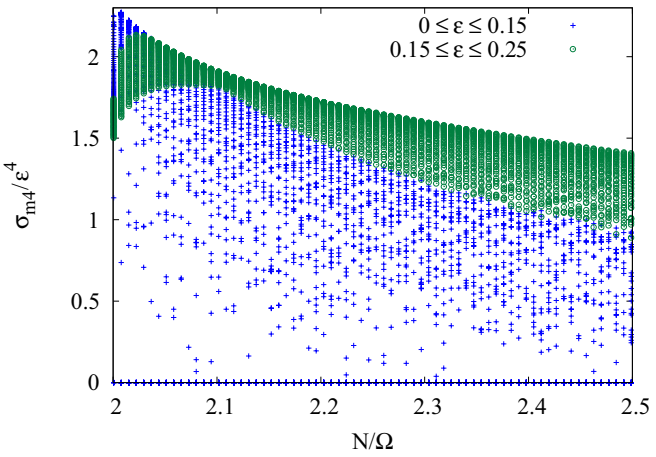


FIG. 11. Destabilizing resonant cases of order $n = 4$. The figure shows the maximal growth rate ($\sigma_{m4}$) of the instability normalized by $\varepsilon^4$ versus $\mathcal{N}$ for $0 \leqslant \varepsilon \leqslant 0.25$.

The destabilizing resonant cases of order $n = 5$, which occur for $2.5 < \mathcal{N}$, are very weaker than those of order $n = 4$. For instance, at $\mathcal{N} = \sqrt{27}/2 \approx 2.598$, the unstable region emanates from the point $[\varepsilon = 0, \mu = \sqrt{2/11} \approx 0.426$ (see Fig. 12)], in agreement with relation Eq. (42). The maximal growth rate of this region of instability is about $\sigma_{m5} \approx 3\varepsilon^5$.

### C. Destabilizing resonances of gravity waves propagating in the $k_3 = 0$ plane

At $k_3 = 0$, the wave numbers $k_1$ and $k_2$ perform a circular motion, $k_1 = k\cos\tau$ and $k_2 = k\cos\tau$, and then one has $k = k_\perp = k_p$ which is time-independent. In that case, i.e., $k_3 = 0$, Eq. (29) with $\hat{\varpi} = 0$ yields $u^{(1)} = 2\varepsilon\mathcal{N}^2(k_2/k)u^{(2)}$. Substituting the later relation together with $k_3 = 0$ into the second and third equations in system Eq. (26), we obtain a two-dimensional Floquet system,

$$d_\tau u^{(2)} = -\frac{1}{\sqrt{1+4\varepsilon^2}}u^{(3)}, \quad d_\tau u^{(3)} = \mathcal{N}^2\left(1 + 4\varepsilon^2\frac{k_2^2}{k^2}\right)u^{(2)}.$$

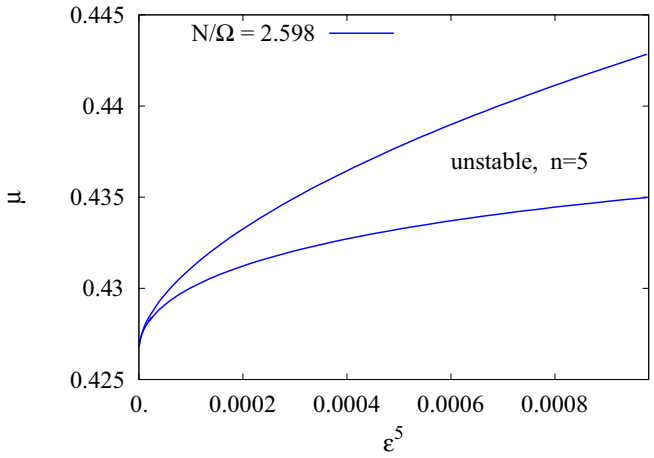


FIG. 12. Destabilizing resonant case of order $n = 5$. Instability band in the $(\varepsilon^5, \mu)$ plane for $\mathcal{N} = \sqrt{27}/2$. The instability emanates from $\mu = 0.426$ and its maximal growth rate is about $\sigma_{m5} \approx 3\varepsilon^5$.

The combination of the later two equations leads to the following Mathieu's equation

$$d_{\tau\tau}u^{(2)} + \frac{\mathcal{N}^2}{\sqrt{1+4\varepsilon^2}}\{1 + 2\varepsilon^2[1 - \cos(2\tau)]\}u^{(2)} = 0. \quad (47)$$

The resonant cases of the gravity waves propagating in the $k_3 = 0$ plane are obtained by setting $\mu = 0$ in Eq. (40), so that, $2\mathcal{N} = n$. We will now prove that only the resonant cases of even order are destabilizing.

By assuming that $\varepsilon \ll 1$ and $\mathcal{N}\varepsilon \ll 1$ and seeking a straightforward expansion for the solution of Eq. (47) in power series of $\varepsilon_1 = \varepsilon^2$ in the form

$$u^{(2)}(\tau, \varepsilon_1) = u_0^{(2)}(\tau) + \varepsilon_1 u_1^{(2)}(\tau) + \varepsilon_1^2 u_2^{(2)}(\tau)\cdots, \quad (48)$$

we prove that the expansion breaks down when $\mathcal{N} = 1, 2, 3, \cdots$ because of the presence of small-divisor terms. For instance, we report here the solution to second order in $\varepsilon$,

$$u^{(2)}(\tau) = A_0\cos(\mathcal{N}\tau + \psi) - \varepsilon^2 A_0\mathcal{N}^2\frac{\cos((\mathcal{N}+2)\tau + \psi)}{4(1+\mathcal{N})} - \varepsilon^2 A_0\mathcal{N}^2\frac{\cos[(\mathcal{N}-2)\tau + \psi]}{4(1-\mathcal{N})} + \cdots, \quad (49)$$

where $A_0$ and $\psi$ are constants. Accordingly, we may conclude that only resonant cases of even order $n$ are destabilizing.

To characterize the instability at and near $\mathcal{N} = 1$, we use the method of multiple scales (see Ref. [52]):

$$\hat{u}^{(2)} = \hat{u}_0^{(2)}(T_0, T_1) + \varepsilon_1\hat{u}_1^{(2)}(T_0, T_1) + \cdots, \quad (50a)$$

$$\mathcal{N}^2 = 1 + \varepsilon_1\delta + \cdots, \quad (50b)$$

where $T_0 = \tau$ (fast timescale) and $T_1 = \varepsilon_1\tau$ (slow timescale) are treated as independent variables. Equation (50b) traduces an expansion of $\mathcal{N}^2$ around the unit value in powers of $\varepsilon_1$. As shown in Appendix D, the solutions are unstable (on timescales of order $\varepsilon^{-2}$) provided $-1 < \delta < 1$. The case where $\delta = \pm 1$ or, equivalently,

$$\mathcal{N} \equiv N/\Omega = 1 \pm \varepsilon^2 \quad (51)$$

(on timescales of order $\varepsilon^{-2}$), characterizes the transition from stability to instability. As for the maximal growth rate $\sigma_{m2}$ of instability, it corresponds to the maximum value of the characteristic exponent $\frac{1}{2}\varepsilon^2\sqrt{1-\delta^2}$, which is reached for $\delta = 0$,

$$\sigma_{m2} = \left[\frac{\varepsilon^2}{2}\sqrt{1-\delta^2}\right]_{\delta=0} = \frac{\varepsilon^2}{2}. \quad (52)$$

Figure 13(a) shows the inviscid instability boundaries in the $(\varepsilon^2, \mathcal{N})$ plane obtained from a numerical integration of Eq. (47). These results well followed the analytical ones, i.e., $\mathcal{N}^2 = 1 \pm \varepsilon^2$, especially for $\varepsilon \leqslant 0.15$. Moreover, at a sufficiently small value of $\varepsilon$, the numerical results indicate that $\sigma_{m2}/\varepsilon^2 \approx 0.5$, in agreement with Eq. (52).

Also, the numerical results indicate that the instability at and near $\mathcal{N} = 2$ is very weak where its maximal growth rate is $\sigma_{m4} \approx 0.95\varepsilon^4$. In the $(\varepsilon^4, \mathcal{N})$ plane, the instability region originates from the point $(0, \mathcal{N} = 2)$ and remains very thin [see Fig. 13(b)]. Note that, when $\varepsilon$ is not very close to zero, the "neutral" curve (characterizing the transition between stability and instability) is below the line $\mathcal{N} = 2$.

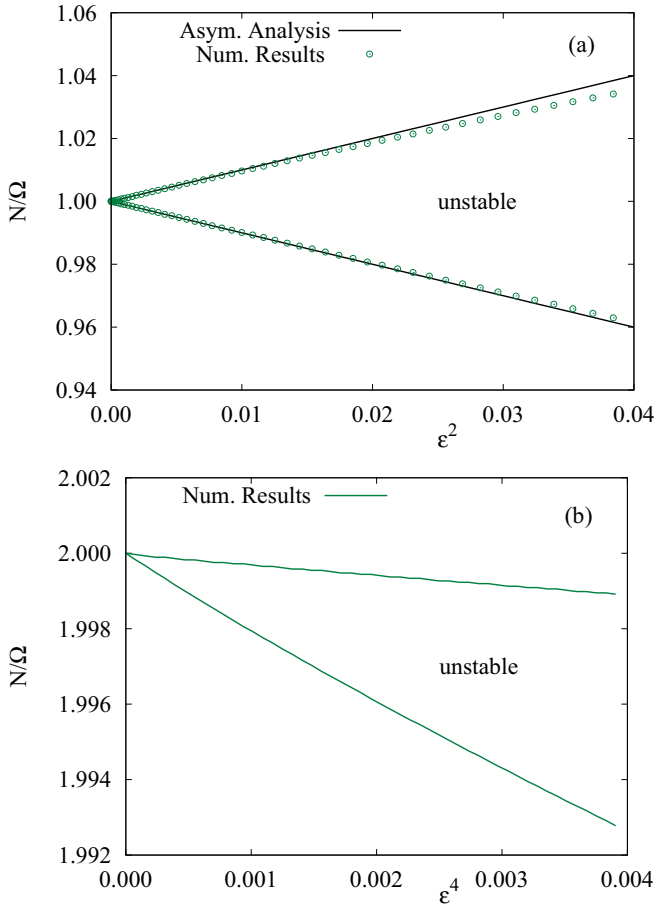


FIG. 13. Destabilizing resonant cases of order $n = 2$ and $n = 4$ of inertia-gravity waves propagating in the $k_3 = 0$ plane. At $k_3 = 0$, instabilities exist only if $n$ is an even integer and $\mathcal{N} = 2n$. The figure shows the instability bands in the $(\mathcal{N}, \varepsilon^2)$ plane [$n = 2$ (a)] and in the $(\mathcal{N}, \varepsilon^4)$ plane [$n = 4$ (b)].

### D. Remarks on the effect of viscosity and the effect of unstable stratification

Of course, weakly growing instabilities will be susceptible to suppression by viscosity and thermal diffusivity. For instance, we consider the case where the diffusivity coefficients are equal, $\nu_v = \kappa$. In that case, the Fourier amplitudes $\hat{\boldsymbol{u}}^{(v)}$ and $\hat{\vartheta}^{(v)}$ of the velocity and buoyancy scalar perturbations may be associated to those in the inviscid limit $\hat{\boldsymbol{u}}$ and $\hat{\vartheta}$ by the substitution

$$(\hat{\boldsymbol{u}}^{(v)}, \hat{\vartheta}^{(v)}) = (\hat{\boldsymbol{u}}, \hat{\vartheta}) \exp\left[-\nu_v \int_0^t k^2(s) ds\right].$$

Accordingly, the maximal growth rate of the instability, if attainable, is

$$\sigma_{mn}^{(v)} = \sigma_{mn} - \mathrm{Re}^{-1}\left(k_p^2 + k_3^2\right) L_0^2 (1 + 4\varepsilon^2 \mu^2), \tag{53}$$

where $\mathrm{Re} = \Omega L_0^2/\nu_v$ is a Reynolds number and $L_0$ is a characteristic length scale. Thus, it can be seen that the effects of viscosity on instabilities are more important at small scales than at large scales. For $L_0\sqrt{k_p^2 + k_3^2} \sim 1$ and $\varepsilon = 0.25$, the destabilizing resonance of order $n = 4$ with $\sigma_{m4} \approx 2\varepsilon^4$, survives to viscous decay if $\mathrm{Re} > 160$.

So far all our analysis has been carried out with $N^2 > 0$. This means that when the mean stratification is alone, it is stabilizing, resulting in neutral dispersive gravity waves and constant PV (toroidal) mode. The case where $N^2 < 0$ is now briefly investigated: the stratification alone is destabilizing, resulting in exponential disturbances, which are no longer waves (e.g., Ref. [22], Chap. 10). If $N^2 < 0$, then the mode with $k_3 = 0$ (or with $\mu = 0$, i.e., the case where the wave vector is perpendicular to the solid-body rotation axis) is always unstable, and its growth rate is $|N|/\Omega$. In counterpart, the modes for which $\mu$ satisfies the inequality

$$0 < \mu_l < \mu \leqslant 1, \quad \mu_l = \sqrt{\frac{-N^2}{4\Omega^2 - N^2}} \tag{54}$$

are stable in the absence of the precession. Here, $\mu_l$ is the value of $\mu$ for which the frequency of the inertia-gravity waves vanishes [see Eq. (38)]. The resonant cases among these stable modes are described by Eq. (40). In view of the above inequality, they are then characterized by

$$0 < \mu_l < \mu = \frac{1}{2}\sqrt{\frac{n^2\Omega^2 - 4N^2}{4\Omega^2 - N^2}} \leqslant 1, \tag{55}$$

where $n = 1, 2, 3, 4$. According to the present numerical computations, these resonant cases are destabilizing except the one of order $n = 4$. However, the mode with $k_3 = 0$ remains the strongest except for small values of $|\mathcal{N}|$ where the maximal growth rate of the subharmonic instability exceeds the one of the mode with $k_3 = 0$,

$$0 < \sigma_m(k_3 = 0) = \frac{|N|}{\Omega} < \sigma_m(n = 1) = \varepsilon \frac{5\sqrt{15}}{8} \frac{\sqrt{\Omega^2 - 4N^2}}{4\Omega^2 - N^2}. \tag{56}$$

For example, for $\varepsilon = 0.2$ and $0 < |N| < 0.123\Omega$, $\sigma_m(n = 1)$ exceeds $|N|/\Omega$.

## V. CONCLUDING REMARKS

We have performed a linear stability analysis of a generic stratified precessing flow. The base flow considered in the present study [see Eq. (5)] constitutes an extension of the one characterizing nonstratified rotating fluid columns subjected to a weak external Coriolis force by Mahalov [12]. In the study of Mahalov [12], it has been shown that an external Coriolis force alters the base flow distorting circular streamlines of the unperturbed rotating columns. He proposed a first order correction to the basic flow, which consists of an exact solution of Euler's equations, namely, $\boldsymbol{U} = (0, \Omega r, -2\varepsilon\Omega r \sin\varphi)$, written in a cylindrical coordinate system (see Appendix A).

The effect of an axial stable density stratification on Taylor columns has been investigated in some experimental and theoretical studies (see, e.g., Refs. [24–26]). Not only the basic velocity but also the basic buoyancy scalar are altered in the case of axially stratified Taylor columns subjected to a Coriolis force. Similar to the analytical developments by Mahalov [12], we have proposed a correction for the basic buoyancy scalar, namely, $\boldsymbol{\nabla}\Theta = N^2(-2\varepsilon\cos\varphi, 2\varepsilon\sin\varphi, 1)$ (see Appendix A).

A physical interpretation of the modified flow has been indicated in Sec. I: the misalignment of the basic "rapid" angular velocity $\boldsymbol{\Omega} = (\boldsymbol{\nabla} \times \boldsymbol{U})(\varepsilon = 0)$ and the precessional one $\boldsymbol{\Omega}_p$, treated as an external Coriolis force, induces a gyroscopic torque. This torque can be exactly balanced by the plane shear or $\boldsymbol{U}_s = (0, 0, -2\varepsilon r\Omega \sin\varphi)$. The induced shear can be shown in previous experimental studies (see, e.g., Refs. [8,16,17]). The presence of the additional horizontal component of the basic buoyancy scalar which vanishes in the case without precession ($\varepsilon = 0$) is thereby caused by the gyroscopic torque as for the additional mean shear.

We have transformed this exact solution of Euler-Boussinesq equations into a Cartesian coordinate system and obtain the so-called Mahalov's base flow [the one described by Eq. (5)]. However, we have shown that, at leading order in $\varepsilon$, the Kerswell's base flow [see Eq. (2)] can be recovered by applying the coordinate transformation given in Sec. IIA2 to the Mahalov's base flow. Note that the Kerswell's base flow [4] has been derived from the so-called Poincaré solution that characterizes the response of an inviscid fluid within a precessing, oblate spheroid.

The disturbances to that base flow are expressed in terms of plane waves, where the direction and the speed of propagation depend on time. The use of PV, which is a Lagrangian invariant for a non diffusive fluid, allowed us to obtain a two-dimensional Floquet system governing the dynamics of disturbances in the linear limit. We have shown that the instability growth rate is the same whether or not PV is zero.

In the limit case $\varepsilon = 0$, the misalignment between the unperturbed buoyancy force and the solid-body rotation axis vanishes (stratification then becomes axial). In this case, they are inertia-gravity waves propagating with frequency $\omega = \pm\sqrt{\omega_r^2 + \omega_g^2}$ ($\omega_r$ and $\omega_g$ are the inertial and gravity frequencies, respectively). The resonant cases of these waves are those for which $2\omega = n\Omega$ ($n$ being an integer number).

For $k_3 = 0$, which corresponds to an infinite wavelength in the axial direction, the frequency of inertial waves is zero and the resonant cases of gravity waves are those where $2N = n\Omega$ ($N$ being the buoyancy frequency). We have proven that the precession ($\varepsilon \neq 0$) destabilizes the resonant cases of even order ($n = 2l$ where $l$ is an integer). The instability at and near $\mathcal{N} \equiv N/\Omega = 1$ has been studied analytically using perturbative techniques [see Sec. III B and Fig. 13(a)]. Its maximal growth rate is $\sigma_{m2} = \varepsilon^2/2$. In counterpart, the instability at and near $\mathcal{N} = 2$, which is very weak, has been investigated numerically. These instabilities are caused by the misalignment between the buoyancy force and the solid-body rotation axis. In the case of an unstable stratification ($N^2 < 0$), the mode $k_3 = 0$ remains the most unstable except for small values of $|N|$ [see Eq. (56)].

We note that, in the case of unbounded elliptical flow [with basic velocity, $\boldsymbol{U} = \Omega(-Ex_2\boldsymbol{e}_1 + E^{-1}x_1\boldsymbol{e}_2)$, where $E \geqslant 1$ is a measure of elliptical deformation of the streamlines], an axial stable stratification does not destabilize the mode $k_3 = 0$. In other words, the resonant cases of gravity waves propagating in the $k_3 = 0$ plane are not destabilized by the ellipticity of the streamlines.

For $k_3 \neq 0$, the destabilizing resonances of inertia-gravity waves by precession are those of order $n \neq 0$. The subharmonic instability (the one corresponding to the resonant cases of order $n = 1$), has been investigated analytically using the perturbative method by Lebovitz and Zweibel [44]. Such an instability gets suppressed by stable stratification when $\mathcal{N}$ exceeds the threshold $\mathcal{N} = 0.5$. The analytical results yielded by the asymptotic analysis at leading order in $\varepsilon$ are in good agreement with the numerical ones (see Figs. 6 and 7). For instance, the maximal growth rate of the subharmonic instability is $\sigma_{m1} = \varepsilon(5\sqrt{15}/8)\sqrt{(1-4\mathcal{N}^2)}/(4-\mathcal{N}^2)$. We indicate that, in the case of the unbounded stratified elliptical flow, the maximal growth rate of subharmonic instability (that associated to the resonant case of order $n = 2$) is $\sigma_{m2} = \varepsilon(9/4)(1-\mathcal{N}^2)/(4-\mathcal{N}^2)$ (see Ref. [18,37]).

The instabilities associated to the resonant cases of order $n = 2, 3, 4, 5$ have been investigated numerically. As suggested by relation Eq. (38) characterizing the resonant cases of inertia-gravity waves, the instabilities of order $n = 2$ and $n = 3$ are suppressed by stratification for $\mathcal{N} > 1$ and $\mathcal{N} > 1.5$, respectively, while the instability of order $n = 4$ exists for all $\mathcal{N}$ and the one of order $n = 5$ appears for $\mathcal{N} > 2.5$. Even if these instabilities are weak, they can survive under the effect of viscosity for high Reynolds number, especially at large scales [see Eq. (53)]. Based on the present parametric study, the effect of nonlinear interactions on the most unstable modes will be investigated by means of DNS in a subsequent paper.

Since the fluid dynamics underlying the dynamo process as a competition between rotation, magnetic fields and the forcing provided by convection and perhaps also precessional or tidal driving (see Ref. [53]), it should be relevant to investigate the destabilizing resonant cases of magneto-inertia-gravity waves by the precession or by the ellipticity of the streamlines. This forms the motivation of a future paper.

## APPENDIX A

### 1. Correction to the base flow of rotating fluid columns subjected to a weak external and stable stratification

Mahalov [12] performed a linear stability analysis of unstratified infinite rotating fluid columns subjected to a weak Coriolis force. He showed that external Coriolis force alters the base flow distorting circular streamlines of the unperturbed rotating fluid columns and proposed a first-order correction to the base flow. In this Appendix, we extend Mahalov's theoretical study by including the effect of stratification.

As indicated in Sec. II A, the instantaneous velocity field $\tilde{\boldsymbol{u}}$ and buoyancy scalar $\tilde{\vartheta}$ satisfy the inviscid Boussinesq's equations [see Eqs. (7)]. Equations (7) are supplemented with boundary conditions. The only boundary condition is that there is no flow through the boundaries [12]. For $\boldsymbol{\Omega}_p = \boldsymbol{0}$, so that $\varepsilon = 0$, one finds that the following form is an exact solution of Eqs. (7):

$$\boldsymbol{U} = V(r)\boldsymbol{e}_\varphi = \Omega r\boldsymbol{e}_\varphi, \quad \Theta = N^2 x_3, \tag{A1}$$

where $(\boldsymbol{e}_r, \boldsymbol{e}_\varphi, \boldsymbol{e}_z)$ is a direct orthonormal basis associated to cylindrical coordinates $(r, \varphi, z \equiv x_3)$. The above solution corresponds to the unperturbed rotating columns under a stable axial stratification. When $\varepsilon \neq 0$, We substitute $\tilde{\boldsymbol{u}} = \boldsymbol{U} + \boldsymbol{u}$ and

$\tilde{\vartheta} = \Theta + \vartheta$ into Eq. (7) written in cylindrical coordinates to obtain the following equations for the perturbation velocity field, $\boldsymbol{u} = (u, v, w)$, perturbation pressure field, $p$, and perturbation buoyancy scalar field, $\vartheta$:

$$\begin{aligned}
\partial_t u + u\partial_r u + \frac{v}{r}\partial_\varphi u + w\partial_z u - \frac{v^2}{r} + \Omega\partial_\varphi u - 2\Omega v &= -\partial_r p + 2\varepsilon\Omega w\sin\varphi + \vartheta m_r \\
\partial_t v + u\partial_r v + \frac{v}{r}\partial_\varphi v + w\partial_z v + \frac{uv}{r} + \Omega\partial_\varphi v + 2\Omega u &= -\frac{1}{r}\partial_\varphi p + 2\varepsilon\Omega w\cos\varphi + \vartheta m_\varphi \\
\partial_t w + u\partial_r w + \frac{v}{r}\partial_\varphi w + w\partial_z w + \Omega\partial_\varphi w &= -\partial_z p - 2\varepsilon\Omega^2 r\cos\varphi - 2\varepsilon\Omega(v\cos\varphi + u\sin\varphi) + \vartheta m_z, \\
\partial_t\vartheta + u\partial_r\vartheta + \frac{v}{r}\partial_\varphi\vartheta + w\partial_e\vartheta + \Omega\partial_\varphi\vartheta + N^2 w = 0, \quad \frac{1}{r}\partial_r(ru) + \frac{1}{r}\partial_\varphi v + \partial_z w &= 0,
\end{aligned} \tag{A2}$$

where $\boldsymbol{m} = (m_r, m_\varphi, m_z)$ is a unit vector that aligns with $\nabla\vartheta$. As in the study by Mahalov, we consider that the perturbation is time-independent, and we expand the velocity, the pressure, and the buoyancy scalar in powers of $\varepsilon$,

$$\begin{aligned}
u &= \varepsilon^2 u_2 + \varepsilon^2 u_3 \cdots, \quad v = \varepsilon^2 v_2 + \varepsilon^2 v_3 \cdots, \\
w &= \varepsilon w_1 + \varepsilon^2 w_2 \cdots, \quad p = \varepsilon^2 p_2 + \varepsilon^2 p_3 \cdots, \\
\vartheta &= \varepsilon\vartheta_1 + \varepsilon^2\vartheta_2 \cdots.
\end{aligned} \tag{A3}$$

For terms of order $\varepsilon$ we have from Eq. (A2)

$$\partial_\varphi w_1 + 2\Omega r\cos\varphi = 0, \tag{A4a}$$

$$\partial_\varphi\vartheta_1 + \frac{N^2}{\Omega} w_1 = 0. \tag{A4b}$$

In the unstratified case ($N^2 = 0$), Mahalov [12] have derived the following solution for $w_1(r, \varphi)$:

$$w_1(r, \varphi) = -2r\Omega\sin\varphi, \tag{A5}$$

and indicated that, in the limit of high Reynolds numbers, $\mathrm{Re} = \Omega^2 R/\nu$ (where $R$ is a characteristic radial lengthscale), the inviscid solution $\boldsymbol{U} = r\Omega\boldsymbol{e}_\varphi - 2\varepsilon\Omega r\sin\varphi\boldsymbol{e}_z$ coincides with the viscous solution in the inner region while differing near the boundaries. Details on the derivation of the solution Eq. (A4) are given in Mahalov [12] and not reported here for the sake of brevity. Accordingly, the integration of Eq. (A4 b) yields the following solution for $\vartheta_1$:

$$\vartheta_1(r, \varphi) = -2N^2 r\sin\varphi + g(r), \tag{A6}$$

where $g(r)$ is an arbitrary function of $r$. By proceeding in a similar manner as in the study by Mahalov [12] [see his analysis after Eq. (4) on p. 893], we show that, in the limit $\mathrm{Re}/\mathrm{Pr} \to +\infty$, the function $g(r)$ vanishes.

Accordingly, the expression of the basic buoyancy scalar $\Theta = N^2(-2\varepsilon r\cos\varphi + z)$, so that

$$\boldsymbol{n} = \frac{\nabla\Theta}{\|\nabla\Theta\|} = \frac{1}{\sqrt{1+4\varepsilon^2}}[-2\varepsilon(\cos\varphi\boldsymbol{e}_r - \sin\varphi\boldsymbol{e}_\varphi) + \boldsymbol{e}_3]$$

is an exact solution of inviscid Boussinesq Eqs. (7).

## APPENDIX B

### 1. Differential system for poloidal, toroidal, and buoyancy modes

In the orthonormal basis $(\boldsymbol{e}^{(1)}, \boldsymbol{e}^{(2)}, \boldsymbol{e}^{(3)})$ defined by Eq. (24), in which the condition $\boldsymbol{k}\cdot\hat{\boldsymbol{u}} = 0$ is satisfied by construction, $\hat{\boldsymbol{u}}$ has only two components, $\hat{\boldsymbol{u}} = \hat{u}_i\boldsymbol{e}_i = u^{(\alpha)}\boldsymbol{e}^{(\alpha)}$ with $i = 1, 2, 3$ and $\alpha = 1, 2$ (the Greek indices take only values 1 or 2), and

$$\boldsymbol{e}^{(1)} = \frac{k_2}{k_\perp}\boldsymbol{e}_1 - \frac{k_1}{k_\perp}\boldsymbol{e}_2, \quad \boldsymbol{e}^{(2)} = \frac{k_1 k_3}{k_\perp k}\boldsymbol{e}_1 + \frac{k_2 k_3}{k_\perp k}\boldsymbol{e}_2 - \frac{k_\perp}{k}\boldsymbol{e}_3.$$

Therefore, Eq. (23a) can be rewritten as

$$\begin{aligned}
d_t\left(u^{(\alpha)}e_i^{(\alpha)}\right) = &-\mathrm{i}\hat{p}k\boldsymbol{e}_i^{(3)} - 2\varepsilon\Omega u^{(\alpha)}(\boldsymbol{e}_1\times\boldsymbol{e}^{(\alpha)})_i \\
&- (\nabla\boldsymbol{U})_{ij}e_j^{(\alpha)} + \hat{\vartheta}n_i,
\end{aligned} \tag{B1}$$

where $e_i^{(\beta)}$ is the component of $\boldsymbol{e}^{(\beta)}$ in the canonical basis $(\boldsymbol{e}_1, \boldsymbol{e}_2, \boldsymbol{e}_3)$. In view of the eikonal equation [i.e., Eq. (20)] and the orthonormal properties, $e_i^{(\alpha)}e_i^{(\beta)} = \delta_{\alpha\beta}$ and $e_i^{(\alpha)}e_j^{(\alpha)} = \delta_{ij}$, it is found that

$$e_i^{(2)}d_t e_i^{(1)} = -e_i^{(1)}d_t e_i^{(2)} = \Omega\left(\frac{k_3}{k} + 2\varepsilon\frac{k_1 k_3^2}{k_\perp^2 k}\right).$$

Therefore, Eq. (B1) can be transformed as

$$\begin{aligned}
d_t u^{(\beta)} = &-u^{(\alpha)}e_i^{(\beta)}d_t e_i^{(\alpha)} \underbrace{-2\varepsilon\Omega u^{(\alpha)}\left(\boldsymbol{e}_1\times\boldsymbol{e}^{(\alpha)}\right)_i e_i^{(\beta)}}_{\text{(I)}} \\
&\underbrace{-e_i^{(\beta)}(\nabla\boldsymbol{U})_{il}e_j^{(\alpha)}u^{(\alpha)}}_{\text{(II)}} + \underbrace{\hat{\vartheta}n_i e_i^{(\beta)}}_{\text{(III)}},
\end{aligned} \tag{B2}$$

where

$$\begin{aligned}
\text{(I)} &= \Omega\frac{k_1}{k}(u^{(2)}, -u^{(1)}), \\
\text{(II)} &= \Omega\left(-\frac{k_3}{k}u^{(2)}, \left(\frac{k_3}{k} - 2\varepsilon\Omega\frac{k_1}{k}\right)u^{(1)} - 2\varepsilon\frac{k_2 k_3}{k^2}u^{(2)}\right), \\
\text{(III)} &= \frac{\Omega}{\sqrt{1+4\varepsilon^2}}\left(-2\varepsilon\frac{k_2}{k_\perp}, \frac{k_\perp}{k} - 2\varepsilon\frac{k_1}{k}\frac{k_3}{k_\perp}\right)u^{(3)},
\end{aligned} \tag{B3}$$

and $u^{(3)} = \hat{\vartheta}/\Omega$. Likewise, we transform Eq. (23b), $d_\tau u^{(3)} = -\mathcal{N}^2\sqrt{1+4\varepsilon^2}\, n_i e_i^{(\alpha)}u^{(\alpha)}$, and obtain the differential system for the toroidal ($u^{(1)}$), poloidal ($u^{(2)}$) modes and buoyancy ($u^{(3)}$) modes [see Eq. (26)].

### 2. Stability of the mode $k_p = 0$

As indicated earlier, both the wave numbers $k_3$ and $k_p = \sqrt{(k_1 + 2\varepsilon k_3)^2 + k_2^2}$ are time-independent. In this Appendix, we show that the mode $k_p = 0$ is unstable for $\varepsilon \geqslant 0.5$. At $k_p = 0$, so that

$$k_1 = -2\varepsilon k_3, \quad k_2 = 0, \quad k_\perp = 2\varepsilon|k_3|, \quad k = |k_3|\sqrt{1+4\varepsilon^2},$$

system Eq. (26) reduces to

$$d_\tau u^{(1)} = \frac{1-4\varepsilon^2}{\sqrt{1+4\varepsilon^2}}\frac{k_3}{|k_3|}u^{(2)}, \quad d_\tau u^{(2)} = -\frac{1}{\sqrt{1+4\varepsilon^2}}\frac{k_3}{|k_3|}u^{(1)},$$

and $d_\tau u^{(3)} = 0$, implying that

$$d_{\tau\tau}u^{(2)} + \left(\frac{1-4\varepsilon^2}{1+4\varepsilon^2}\right)u^{(2)} = 0.$$

Hence, the solution of the above second-order ordinary differential equation is unstable for $\varepsilon \geqslant 0.5$.

## APPENDIX C

### 1. The asymptotic method by Lebovitz and Zweibel

In this Appendix, we use the asymptotic method of Lebovitz and Zweibel [44] (see also Ref. [54]) to determine, at leading order in $\varepsilon$, the maximal growth rate of the solution of the two-dimensional Floquet system Eq. (30), $d_\tau \hat{\boldsymbol{u}} = \mathbf{D}\cdot\hat{\boldsymbol{u}}$. Recall that $\boldsymbol{\Phi}(\tau, \varepsilon, \mu, \mathcal{N})$ denotes the fundamental matrix solution,

$$d_\tau \boldsymbol{\Phi} = \mathbf{D}\cdot\boldsymbol{\Phi}, \quad \boldsymbol{\Phi}(\tau = 0) = \mathbf{I}_2, \tag{C1}$$

and $\mathbf{M} = \boldsymbol{\Phi}(2\pi, \varepsilon, \mu, \mathcal{N})$ the Floquet multiplier matrix where its determinant is unity (see the end of Sec. II C). It follows that whenever $\lambda$ is an eigenvalue of $\mathbf{M}$, so also are its inverse $\lambda^{-1}$ and its complex conjugate $\lambda^*$ (see also Ref. [44]). We denote by $\mathrm{p}(\lambda, \varepsilon) = |\mathbf{M} - \lambda\mathbf{I}_2|$ the characteristic polynomial of $\mathbf{M}$ and by $\Lambda_1$ and $\Lambda_2$ its roots. A necessary condition for stability is that each root lie on the unit circle.

### 2. Expansion in Taylor series of the Floquet multiplier matrix

We expand the Floquet multiplier matrix $\mathbf{M}(\varepsilon, \mu, \mathcal{N})$ in Taylor series in the neighborhood of $(\varepsilon, \mu) = (0, \mu_0)$, holding $\mathcal{N}$ constant,

$$\mathbf{M} = \mathbf{M}_0(\mu_0, 0) + \varepsilon\mathbf{M}_\varepsilon(\mu_0, 0) + (\mu - \mu_0)\mathbf{M}_\mu(\mu_0, 0) + \cdots, \tag{C2}$$

where $\mathbf{M}_\varepsilon = (\partial\mathbf{M}/\partial\varepsilon)$, $\mathbf{M}_\mu = (\partial\mathbf{M}/\partial\mu)$ and the dots indicate higher-order terms in $\varepsilon$ and $\mu - \mu_0$. Generally, at sufficiently small $\varepsilon$, the region in the the $(\varepsilon, \mu)$ plane where instability occurs is typically a wedge with apex at a point $(\varepsilon, \mu) = (0, \mu_0)$ and boundaries

$$\mu = \mu_0 + \nu_\pm\varepsilon, \tag{C3}$$

where the slopes $\nu_+$ and $\nu_-$ are to be found. Therefore, Eq. (C2) can be rewritten as

$$\mathbf{M} = \mathbf{M}_0 + \varepsilon\mathbf{M}_1 + \mathcal{O}(\varepsilon^2), \quad \mathbf{M}_1 = \mathbf{M}_\varepsilon + \nu\mathbf{M}\mu. \tag{C4}$$

Accordingly, we no longer need the designation $\mu_0$ and, hereinafter, use the symbol $\mu$ in its place.

To determine matrices $\mathbf{M}_0$, $\mathbf{M}_\varepsilon$, and $\mathbf{M}_\mu$, we expand, for a given $\tau \in [0, 2\pi]$, $\boldsymbol{\Phi}$ and $\mathbf{D}$,

$$\boldsymbol{\Phi}(\tau, \varepsilon) = \boldsymbol{\Phi}_0(\tau, \mu, 0) + \varepsilon\boldsymbol{\Phi}_1(\tau, \mu, 0) + \mathcal{O}(\varepsilon^2), \tag{C5a}$$

$$\mathbf{D}(\tau, \varepsilon) = \mathbf{D}_0 + \varepsilon\mathbf{D}_\varepsilon(\tau, 0) + \mathcal{O}(\varepsilon^2), \tag{C5b}$$

where $\boldsymbol{\Phi}_0(\tau = 0) = \mathbf{I}_2$ and $\boldsymbol{\Phi}_1(\tau = 0) = \mathbf{0}$. Substituting Eq. (C5) into Eq. (C1), we obtain

$$d_\tau\boldsymbol{\Phi}_0 = \mathbf{D}_0\cdot\boldsymbol{\Phi}_0, \quad d_\tau\boldsymbol{\Phi}_1 = \mathbf{D}_0\cdot\boldsymbol{\Phi}_1 + \mathbf{D}_\varepsilon\cdot\boldsymbol{\Phi}_0,$$

with solution $\boldsymbol{\Phi}_0(\tau) = \mathrm{e}^{\tau\mathbf{D}_0}$ and

$$\boldsymbol{\Phi}_1(\tau) = \boldsymbol{\Phi}_0\cdot\left[\int_0^\tau \boldsymbol{\Phi}_0^{-1}(s)\cdot\mathbf{D}_\varepsilon(s)\cdot\boldsymbol{\Phi}_0(s)ds\right]. \tag{C6}$$

Because the characteristic polynomial $\mathrm{p}(\lambda, \varepsilon)$ is the same in any coordinate system and the two eigenvalues of the matrix $\mathbf{D}_0$, given by Eq. (38), are distinct $\sigma_{1,2} = \pm\mathrm{i}\sqrt{(4-\mathcal{N}^2)\mu^2 + \mathcal{N}^2} \neq 0$ with $\mu \neq 0$, we transform the solution in the base diagonalizing $\mathbf{D}_0$,

$$\tilde{\mathbf{D}}_0 = \mathbf{T}^{-1}\cdot\mathbf{D}_0\cdot\mathbf{T} = \mathrm{diag}(\sigma_1, -\sigma_1), \tag{C7}$$

where the columns of $\mathbf{T}$ are the eigenvectors of $\mathbf{D}_0$,

$$\mathbf{T} = \frac{1}{2\mu}\begin{pmatrix} 2\mu & 2\mu \\ \sigma_1 & -\sigma_1 \end{pmatrix}, \quad \mathbf{T}^{-1} = \frac{1}{2\sigma_1}\begin{pmatrix} \sigma_1 & 2\mu \\ \sigma_1 & -2\mu \end{pmatrix}. \tag{C8}$$

Therefore, in the base diagonalizing $\mathbf{D}_0$, $\tilde{\mathbf{M}}_0$ and $\tilde{\mathbf{M}}_\varepsilon$ take the form

$$\tilde{\mathbf{M}}_0 = \mathbf{T}^{-1}\cdot\mathbf{M}_0\cdot\mathbf{T} = \mathrm{diag}(\mathrm{e}^{2\pi\sigma_1}, \mathrm{e}^{-2\pi\sigma_1}), \tag{C9a}$$

$$\tilde{\mathbf{M}}_\varepsilon = \mathbf{T}^{-1}\cdot\mathbf{M}_\varepsilon\cdot\mathbf{T} = \tilde{\mathbf{M}}_0\cdot\tilde{\mathbf{J}}, \tag{C9b}$$

$$\tilde{J}_{ij} = (\mathbf{T}^{-1})_{im}T_{lj}\int_0^{2\pi}\mathrm{e}^{(\sigma_j-\sigma_i)\tau}(\mathbf{D}_\varepsilon)_{ml}(\tau)d\tau. \tag{C9c}$$

To complete the construction of the matrix $\tilde{\mathbf{M}}_1$, which appears in Eq. (C4), we need the derivative of $\tilde{\mathbf{M}}_0(\mu) = \tilde{\mathbf{M}}(\mu, 0) = \mathrm{diag}(\mathrm{e}^{2\pi\sigma_1}, \mathrm{e}^{-2\pi\sigma_1})$, with respect to $\mu$,

$$\tilde{\mathbf{M}}_\mu(\mu, 0) = -2\pi\frac{(4-\mathcal{N}^2)\mu}{\sigma_1}\mathrm{diag}(\mathrm{e}^{2\pi\sigma_1}, -\mathrm{e}^{-2\pi\sigma_1}). \tag{C10}$$

The elements $(\tilde{\mathbf{M}})_{ij}$ are calculated in Appendix C3.

### 3. Expansion of the characteristic polynomial

We expand the characteristic polynomial in Taylor series around $\varepsilon = 0$ to second order in $\varepsilon$,

$$\mathrm{p}(\lambda, \varepsilon) = \mathrm{p}_0(\lambda) + \mathrm{p}_1(\lambda)\varepsilon + \mathrm{p}_2(\lambda)\varepsilon^2 + \mathcal{O}(\varepsilon^3), \tag{C11}$$

where $\mathrm{p}_0(\lambda)$ is the characteristic polynomial of $\mathbf{M}_0$ with roots $\lambda_1 = \mathrm{e}^{2\pi\sigma_1}$ and $\lambda_2 = \mathrm{e}^{2\pi\sigma_2} = \mathrm{e}^{-2\pi\sigma_1}$, so that, $\lambda_1 = \lambda_2$ for $\sigma_1 - \sigma_2 = \pm\mathrm{i}n$ ($n$ being an integer). Thus, one can obtain the roots of $\mathrm{p}(\lambda, \varepsilon)$ in the form of a Puiseux expansion (see Hille [55])

$$\Lambda_1 = \lambda_1 + \varepsilon^{\frac{1}{2}}\beta_{\frac{1}{2}} + \varepsilon\beta_1 + \mathcal{O}(\varepsilon^{\frac{3}{2}}),$$

where $\beta_{\frac{1}{2}}^2 = -2\mathrm{p}_1(\lambda_1)/(d^2\mathrm{p}_0/d\lambda^2)(\lambda_1)$ and $\beta_1$ can be established from the quadratic equation (see Eq. (32) in Ref. [44])

$$\frac{1}{2}\left[\frac{d^2\mathrm{p}_0}{d\lambda^2}(\lambda_1)\right]\beta_1^2 + \left[\frac{d\mathrm{p}_1}{d\lambda}(\lambda_1)\right]\beta_1 + \mathrm{p}_2(\lambda_1) = 0. \tag{C12}$$

By the use of the formulas for the derivatives of the characteristic polynomial with respect to parameter $\varepsilon$, derived by Lebovitz and Zweibel [44] (see their Appendix B), we obtain

$$\mathrm{p}_1(\lambda_1) = 0, \quad \frac{d^2\mathrm{p}_0}{d\lambda^2}(\lambda_1) = 2,$$
$$\frac{d\mathrm{p}_1}{d\lambda}(\lambda_1) = (\tilde{\mathbf{M}}_1)_{11} + (\tilde{\mathbf{M}}_1)_{22},$$
$$\mathrm{p}_2(\lambda_1) = \begin{vmatrix} (\tilde{\mathbf{M}}_1)_{11} & (\tilde{\mathbf{M}}_1)_{12} \\ (\tilde{\mathbf{M}}_1)_{21} & (\tilde{\mathbf{M}}_1)_{22} \end{vmatrix}. \tag{C13}$$

Defining $\alpha = \beta_1/\lambda_1$. Either $\alpha$ is pure-imaginary and we infer stability (to leading order in $\varepsilon$), or $\Re\alpha \neq 0$ and we infer instability (see Proposition 2 in Lebovitz and Zweibel [44]).

#### 4. Characterization of the subharmonic instability

From Eq. (30) giving the matrix $\mathbf{D}$, we deduce $\mathbf{D}_\varepsilon$,

$$(\mathbf{D}_\varepsilon)_{11} = \mathrm{i}\mathcal{N}^2\frac{\sqrt{1-\mu^2}}{2\mu}(\mathrm{e}^{\mathrm{i}\tau} - \mathrm{e}^{-\mathrm{i}\tau}),$$
$$(\mathbf{D}_\varepsilon)_{12} = \frac{2\mu^2(1-\mu^2)+1}{\sqrt{1-\mu^2}}(\mathrm{e}^{\mathrm{i}\tau} + \mathrm{e}^{-\mathrm{i}\tau}),$$
$$(\mathbf{D}_\varepsilon)_{21} = \frac{-1}{2\sqrt{1-\mu^2}}[6\mu^2 - 4\mu^4 + \mathcal{N}^2(1-\mu^2)^2] \times (\mathrm{e}^{\mathrm{i}\tau} + \mathrm{e}^{-\mathrm{i}\tau}),$$
$$(\mathbf{D}_\varepsilon)_{22} = \mathrm{i}\frac{\sqrt{1-\mu^2}}{2\mu}(2\mu^2 - \mathcal{N}^2)(\mathrm{e}^{\mathrm{i}\tau} - \mathrm{e}^{-\mathrm{i}\tau}). \tag{C14}$$

This implies that $\int_0^{2\pi} \mathrm{e}^{(\sigma_j-\sigma_i)\tau}\mathbf{D}_\varepsilon d\tau = \mathbf{0}$ if $\sigma_j - \sigma_i \neq \pm\mathrm{i}$, and hence, the diagonal elements $\tilde{J}_{11}$ and $\tilde{J}_{22}$ given by Eq. (C9) are zero. For $\sigma_j - \sigma_i = \pm\mathrm{i}$, the expression of $\tilde{J}_{12}$ given by Eq. (C9c) can be rewritten as follows:

$$\tilde{J}_{12} = (\mathbf{T}^{-1})_{1m}T_{n2}\int_0^{2\pi}\mathrm{e}^{-\mathrm{i}\tau}(\mathbf{D}_\varepsilon)_{mn}d\tau = (\mathbf{T}^{-1})_{1m}T_{n2}H^+_{mn},$$

where

$$H^+_{11} = \mathrm{i}\pi\frac{\mathcal{N}^2(1-\mu^2)}{\mu\sqrt{1-\mu^2}},$$
$$H^+_{12} = \frac{2\pi\mu}{\mu\sqrt{1-\mu^2}}[2\mu^2(1-\mu^2)+1],$$
$$H^+_{21} = -\frac{\mu\pi}{\mu\sqrt{1-\mu^2}}[6\mu^2 - 4\mu^4 + \mathcal{N}^2(1-\mu^2)^2],$$
$$H^+_{22} = -\mathrm{i}\pi\frac{(1-\mu^2)}{\mu\sqrt{1-\mu^2}}(\mathcal{N}^2 - 2\mu^2). \tag{C15}$$

By replacing $\sigma_1$ by $\mathrm{i}/2$ in Eq. (C8) giving the matrices $\mathbf{T}$ and $\mathbf{T}^{-1}$, we find

$$\tilde{J}_{12} = \frac{\mathrm{i}\pi}{4\mu\sqrt{1-\mu^2}}[1+2\mu^2(1-\mu^2)][4\mathcal{N}^2(1-\mu^2)-1] - \frac{\mathrm{i}\pi}{4\mu\sqrt{1-\mu^2}}[4\mu^2(1-13\mu^2+8\mu^4)]. \tag{C16}$$

The later expression can be further simplified by using the resonance condition, $\sigma_1 - \sigma_2 = \pm\mathrm{i}$, or equivalently,

$$4\mathcal{N}^2(1-\mu^2) = 1 - 16\mu^2, \tag{C17}$$

so that

$$\tilde{J}_{12} = -\mathrm{i}\pi 5\mu\sqrt{1-\mu^2}. \tag{C18}$$

In a similar manner, we calculate $\tilde{J}_{21}$

$$\tilde{J}_{21} = (\mathbf{T}^{-1})_{2m}T_{n1}\int_0^{2\pi}\mathrm{e}^{\mathrm{i}\tau}(\mathbf{D}_\varepsilon)_{mn}d\tau = (\mathbf{T}^{-1})_{2m}T_{n1}H^-_{mn},$$

where

$$H^-_{11} = -H^+_{11}, \quad H^-_{12} = H^+_{12}, \quad H^-_{21} = H^+_{21} \quad H^-_{22} = -H^+_{22}.$$

We find that $\tilde{J}_{21} = -\tilde{J}_{12}$. Accordingly, with the help of Eq. (C10), in which we replace $\sigma_1$ by $\mathrm{i}/2$, and the expression found for $\tilde{J}_{ij}$ we determine the matrix $\tilde{\mathbf{M}}_1$ given by the second relation of Eq. (C4),

$$\lambda_1{}^{-1}(\tilde{\mathbf{M}}_1)_{11} = -\lambda_1{}^{-1}(\tilde{\mathbf{M}}_1)_{22} = 4i\pi(4-\mathcal{N}^2)\mu\nu,$$
$$\lambda_1{}^{-1}(\tilde{\mathbf{M}}_1)_{12} = -\lambda_1{}^{-1}(\tilde{\mathbf{M}}_1)_{21} = -\mathrm{i}\pi 5\mu\sqrt{1-\mu^2}, \tag{C19}$$

where $\lambda_1 = \mathrm{e}^{2\pi\sigma_1} = -1$ for $\sigma_1 = \mathrm{i}/2$. Finally, in view of Eqs. (C12), (C13), and (C19), the quadratic equation for $\alpha = \beta_1/\lambda_1 = -\beta_1$ takes the form

$$\alpha^2 + [4\pi(4-\mathcal{N}^2)\mu\nu]^2 - [5\pi\mu\sqrt{1-\mu^2}]^2 = 0. \tag{C20}$$

This has a maximum instability increment (when $\nu = 0$) given by

$$\sigma_{m1} = \frac{\varepsilon}{2\pi}(\Re\alpha)_{\max} = \frac{5}{2}\varepsilon\mu\sqrt{1-\mu^2}. \tag{C21}$$

Replace $\mu$ by its expression deduced from Eq. (C17)

$$\mu = \frac{1}{2}\sqrt{\frac{1-4\mathcal{N}^2}{4-\mathcal{N}^2}},$$

it comes

$$\sigma_{m1} = \varepsilon\frac{5\sqrt{15}}{8}\frac{\sqrt{1-4\mathcal{N}^2}}{(4-\mathcal{N}^2)}. \tag{C22}$$

This subharmonic instability has a bandwidth $(\nu_+ - \nu_-)\varepsilon$ that is, for given $\varepsilon$ and $\mathcal{N}$, the length of the $\mu$ interval for which the unperturbed configuration is unstable (see Ref. [44]). It is determined by the values of that make the real part of $\alpha$ vanish, so that

$$\nu_\pm = \pm\frac{5\sqrt{1-\mu^2}}{4(4-\mathcal{N}^2)} = \pm\frac{5\sqrt{15}}{64}\left(1 - \frac{\mathcal{N}^2}{4}\right)^{-\frac{3}{2}}. \tag{C23}$$

## APPENDIX D

### 1. Destabilizing resonant cases at $k_3 = 0$: A solution at and near $N/\Omega = 1$

In this Appendix, we show that, at and near $\mathcal{N} \equiv N/\Omega = 1$, the solution of the Hill's Eq. (47), governing the evolution of $u^{(2)}$ in the $k_3 = 0$ plane, is unstable. As indicated previously, we use the method of multiple scales (see Ref. [52]). We denote by $\partial_0$ (respectively, by $\partial_1$) the partial derivative with respect to the variable $T_0 = \Omega t$ (respectively, $T_1 = \varepsilon\Omega t$).

Substituting the expansion given by Eq. (50) for $u^{(2)}$ into Hill's Eq. (47) gives

$$0 = \left(\partial_{00}u_0^{(2)} + u_0^{(2)}\right) + \varepsilon_1\left[\partial_{00}u_1^{(2)} + u_1^{(2)} + 2\partial_{01}u_0^{(2)} + \delta u_0^{(2)} + 2u_0^{(2)}\cos(2T_0)\right] + \cdots, \tag{D1}$$

where the expansion $(1+4\varepsilon^2)^{-\frac{1}{2}} = 1 - 2\varepsilon_1 + \cdots$ has been used. Equating each of the coefficients of $\varepsilon_1^0$ and $\varepsilon_1$, we obtain

$$\partial_{00}\hat{u}_0^{(2)} + \hat{u}_0^{(2)} = 0, \tag{D2a}$$

$$\partial_{00}\hat{u}_1^{(2)} + \hat{u}_1^{(2)} = -2\partial_{01}\hat{u}_0^{(2)} - \delta\hat{u}_0^{(1)} + 2\hat{u}_0^{(1)}\cos(2T_0). \tag{D2b}$$

The leading order solution reads

$$u_0^{(2)} = A(T_1)e^{iT_0} + A^*(T_1)e^{-iT_0},$$

where $A^*(T_1)$ denotes the conjugate. Substituting the later solution into Eq. (D2b), we obtain

$$\partial_{00}u_1^{(2)} + u_1^{(2)} = (-2i\partial_1 A - \delta A + A^*)e^{iT_0} + (2i\partial_1 A^* - \delta A^* + A)e^{-iT_0} + Ae^{3iT_0} + A^*e^{-3iT_0}. \tag{D3}$$

Thus, the secular terms in $\hat{u}_1^{(2)}$ are zero if

$$-2i\partial_1 A - \delta A + A^* = 0,$$

or equivalently, by setting $A = \alpha(T_1) + i\beta(T_1)$, if

$$\partial_1\alpha = -\tfrac{1}{2}(\delta+1)\beta \quad \text{and} \quad \partial_1\beta = \tfrac{1}{2}(\delta-1)\alpha. \tag{D4}$$

The integration of the above system gives

$$\alpha(T_1) = A_1 e^{\frac{1}{2}\sqrt{1-\delta^2}T_1} + A_2 e^{-\frac{1}{2}\sqrt{1-\delta^2}T_1},$$

where $A_1$ and $A_2$ are constants. Thus, the solution is unstable if $-1 < \delta < 1$.


[1] F. H. Busse, Steady fluid flow in a precessing spheroidal shell, J. Fluid Mech. **33**, 739 (1968).

[2] W. V. R. Malkus, Precession of the Earth as the cause of geomagnetism: Experiments lend support to the proposal that precessional torques drive the Earth's dynamo, Science **160**, 259 (1968).

[3] J. Vanyo and P. Likins, Measurement of energy dissipation in a liquid-filled, precessing, spherical cavity, Trans. ASME: J. Appl. Mech. **38**, 674 (1971).

[4] R. R. Kerswell, The instability of precessing flow, Geophys. Astrophys. Fluid Dyn. **72**, 107 (1993).

[5] A. Tilgner, Magnetohydrodynamic flow in precessing spherical shells, J. Fluid Mech. **379**, 303 (1999).

[6] J. Noir, D. Brito, K. Aldridge, and P. Cardin, Experimental evidence of inertial waves in a precessing spheroidal cavity, Geophys. Res. Lett. **28**, 3785 (2001).

[7] S. Lorenzani and A. Tilgner, Inertial instabilities of fluid flow in precessing spheroidal shells, J. Fluid Mech. **492**, 363 (2003).

[8] W. Mouhali, T. Lehner, J. Léorat, and R. Vitry, Evidence for a cyclonic regime in a precessing cylindrical container, Exp. Fluids **53**, 1693 (2012).

[9] K. Komoda and S. Goto, Three-dimensional flow structures of turbulence in precessing spheroids, Phys. Rev. Fluids **4**, 014603 (2019).

[10] J. Herault, T. Gundrum, A. Giesecke, and F. Stefani, Subcritical transition to turbulence of a precessing flow in a cylindrical vessel, Phys. Fluids **27**, 124102 (2015).

[11] K. Glampedakis, N. Andersson, and D. I. Jones, On the Stability of Precessing Superfluid Neutron Stars, Phys. Rev. Lett. **100**, 081101 (2008).

[12] A. Mahalov, The instability of rotating fluid columns subjected to a weak external Coriolis force, Phys. Fluids A **5**, 891 (1993).

[13] E. B. Gledzer, F. V. Dolzhansky, A. M. Obukhov, and V. M. Ponomarev, An experimental and theoretical study of the stability of motion of a liquid in an elliptical cylinder, Isv. Atmos. Ocean. Phys. **11**, 617 (1975).

[14] F. A. Waleffe, The 3D instability of a strained vortex and its relation to turbulence, Ph.D. thesis, MIT, 1989.

[15] A. Salhi and C. Cambon, Precessing rotating flows with additional shear: Stability analysis, Phys. Rev. E **79**, 036303 (2009).

[16] A. Vladimirov and V. F. Tarasov, On the forced regimes of rotating fluid motion, Sov. Phys. DoM. **30**, 654 (1985).

[17] R. J. Wiener, P. W. Hammer, C. E. Swanson, and R. J. Donnelly, Stability of Taylor-Couette flow Subject to an External Coriolis Force, Phys. Rev. Lett. **64**, 1115 (1990).

[18] R. R. Kerswell, Elliptical instability, Annu. Rev. Fluid Mech. **34**, 83 (2002).

[19] W. Malkus, Energy sources for planetary dynamos, in *Lectures on Solar and Planetary Dynamos*, edited by M. Proctor and A. Gilbert (Publications of the Newton Institute, Cambridge University Press, Cambridge, 1994), pp. 161–180.

[20] B. J. Bayly, Three-Dimensional Instability of Elliptical Flow, Phys. Rev. Lett. **57**, 2160 (1986).

[21] A. D. D. Craik and W. O. Criminale, Evolution of wavelike disturbances in shear flows: A class of exact solutions of the Navier-Stokes equations, Proc. R. Soc. London A **406**, 13 (1986).

[22] P. Sagaut and C. Cambon, *Homogeneous Turbulence Dynamics* (Cambridge University Press, Cambridge, 2008).

[23] A. Lifschitz and E. Hameiri, Local stability conditions in fluid dynamics, Phys. Fluids **3**, 2644 (1991)

[24] P. A. Davies, Experiments on Taylor columns in rotating stratified fluids, J. Fluid Mech. **54**, 691 (1972).

[25] B. Caton, B. Janiaud, and E. J. Hopfinger, Stability and bifurcations in stratified Taylor-Couette flow, J. Fluid Mech. **419**, 93 (2000).

[26] R. Hollerbach, Instabilities of Taylor columns in a rotating stratified fluid, Phys. Lett. A **373**, 3775 (2009).

[27] A. D. D. Craik, The stability of unbounded two- and three-dimensional flows subject to body forces: Some exact solutions, J. Fluid Mech. **198**, 275 (1989).

[28] X. Wei and A. Tilgner, Stratified precessional flow in spherical geometry, J. Fluid Mech. **718**, R2-1 (2013).

[29] J. Vormann and U. Hansen, Characteristics of a precessing flow under the influence of a convecting temperature field in a spheroidal shell, J. Fluid Mech. **891**, A15 (2020).

[30] R. T. Pierrehumbert, Universal Short-Wave Instability of Two-Dimensional Eddies in an Inviscid Fluid, Phys. Rev. Lett. **57**, 2157 (1986).

[31] S. A. Balbus and J. F. Hawley, Instability, turbulence, and enhanced transport in accretion disks, Rev. Mod. Phys. **70**, 1 (1998).

[32] A. Salhi, T. Lehner, F. Godeferd and C. Cambon, Magnetized stratified rotating shear waves, Phys. Rev. E **85**, 026301 (2012).

[33] P. Goldreich and D. Lynden-Bell, Spiral arms as sheared gravitational instabilities, Mon. Not. R. Astron. Soc. **130**, 125 (1965).

[34] A. J. Barker, On turbulence driven by axial precession and tidal evolution of the spin-orbit angle of close-in giant planets, Mon. Not. R. Astron. Soc. **460**, 2339 (2016).

[35] A. Khlifi, A. Salhi, S. Nasraoui, F. Godeferd, and C. Cambon, Spectral energy scaling in precessing turbulence, Phys. Rev. E **98**, 011102(R) (2018).

[36] A. Salhi, A. Khlifi, and C. Cambon, Nonlinear effects on the precessional instability in magnetized turbulence, Atmosphere **11**, 14 (2020).

[37] T. Miyazaki and Y. Fukumoto, Three-dimensional instability of strained vortices in a stably stratified fluid, Phys. Fluids A **4**, 2515 (1992).

[38] P. Otheguy, J.-M. Chomaz, and P. Billant, Elliptic and zigzag instabilities on co-rotating vertical vortices in a stratified fluid, J. Fluid Mech. **553**, 253 (2006).

[39] D. Guimbard, S. Le Dizès, M. Le Bars, P. Le Gal, and S. Leblanc, Elliptic instability of a stratified fluid in a rotating cylinder, J. Fluid Mech. **660**, 240 (2010).

[40] S. Suzuki, M. Hirota, and Y. Hattori, Strato-hyperbolic instability: A new mechanism of instability in stably stratified vortices, J. Fluid Mech. **854**, 293 (2018).

[41] S. Singh and M. Mathur, Effects of Schmidt number on the short-wavelength instabilities in stratified vortices, J. Fluid Mech. **867**, 765 (2019).

[42] J. Pedlowsky, *Geophysical Fluid Dynamics* (Springer Verlag, New York/Berlin/Heidelberg, 1987).

[43] A. H. Nayfeh, *Perturbation Methods* (Wiley-VCH Verlag GmbH & Co. KGaA, Weinheim, 2004).

[44] N. R. Lebovitz and E. Zweibel, Magnetoelliptic instabilities, Astrophys. J. **609**, 301 (2004).

[45] P. A. Davidson, *An Introduction to Magnetohydrodynamics* (Cambridge University Press, Cambridge, 2013).

[46] J. Slane and S. Tragesser, Analysis of periodic nonautonomous inhomogeneous systems, Nonlinear Dynam. Syst. Theory **11**, 183 (2011).

[47] P. A. Kuchment, *Floquet Theory for Partial Differential Equations.* Operator Theory: Advances and Applications, Vol. 60 (Birkhäuser Verlag, Bessel/Boson/Berlin, 1993).

[48] R. Marino, A. Pouquet, and D. Rosenberg, Resolving the Paradox of Oceanic Large-Scale Balance and Small-Scale Mixing, Phys. Rev. Lett. **114**, 114504 (2015).

[49] L. M. Smith and F. Waleffe, Generation of slow large scales in forced rotating stratified turbulence, J. Fluid Mech. **451**, 145 (2002).

[50] R. Marino, P. D. Mininni, D. Rosenberg, and A. Pouquet, Inverse cascades in rotating stratified turbulence: Fast growth of large scales, Europhys. Lett. **102**, 44006 (2013).

[51] A. Pouquet, R. Marino, P. D. Mininni, and D. Rosenberg, Dual constant-flux energy cascades to both large scales and small scales, Phys. Fluids **29**, 111108 (2017).

[52] P. Glendinning, *Stability, Instability and Chaos: An Introduction to the Theory of Nonlinear Differential Equations* (Cambridge University Press, Cambridge, UK, 1994).

[53] C. C. Finlay, M. Dumberry, A. Chulliat, and M. A. Pais, Short timescale core dynamics: Theory and observations, Space Sci. Rev. **155**, 177 (2010).

[54] A. Salhi and S. Nasraoui, Instability of subharmonic resonances in magnetogravity shear waves, Phys. Rev. E **88**, 063016 (2013).

[55] E. Hille, *Analytic Function Theory*, Vol. 2 (Ginn, New York, 1962).